TECHNIQUES FOR USING AGGREGATE CURRENT MEASUREMENTS TO DETECT FAULTS IN MULTIPLE INDUCTION MACHINES

by

Poripsa Chakrabarty

A thesis submitted to the faculty of
The University of North Carolina at Charlotte
in partial fulfillment of the requirements
for the degree of Master of Science in
Electrical Engineering

Charlotte

2017

Approved by:

_____
Dr. Robert Cox

_____
Dr. Andrew Willis

_____
Dr. Valentina Cecchi

_____
Dr. Yawo H. Amengonu

ABSTRACT

PORIPSA CHAKRABARTY. Techniques for using aggregate current measurements to detect faults in multiple induction machines. (Under the direction of DR. ROBERT COX)

Due to induction motor's properties of resilience, durability and cost effectiveness they are the most widely used electrical transducers across all industries. Naturally, because of these properties of ruggedness they are often selected for use in harsh conditions increasing their risk of mechanical wear and tear. Almost 80% of all drives across industries are induction motors [1], due to which they end up consuming almost 40% to 50% of a country's total generating capacity (power) [2]. Hence it is vital that the induction motors run to their maximum efficiency to avoid loss of revenue and power. Over time, a number of methods and techniques have been developed to monitor health of the motor and for fault diagnosis.

Usage of such methods however has led to increased cost to the industry as most of the techniques employed need to have equipment on every motor individually to gain valuable and necessary data. Moreover they would also require skilled man-power to be able to correctly use these methods. Hence to mitigate the cost and man-hours required for diagnostics of induction motors, a possible way to perform such diagnostics on multiple motors simultaneously was inquired by EPRI (Electric Power Research Institute).

This thesis answers the question by providing a way to perform electrical diagnostics on multiple motors simultaneously by being able to distinguish between two motor signals measured from a common power source(the source is split to feed the motors in parallel). The process outlined in the thesis comprises of estimating individual rotor eccentricity frequency of the motors and their corresponding amplitudes for fault detection.

ACKNOWLEDGEMENTS

I would like to thank Dr Cox for his invaluable insights and help. I would also like to thank EPRI for funding this thesis and for their continued work in improving industries by their research.

TABLE OF CONTENTS

LIST OF FIGURES vii

LIST OF TABLES x

LIST OF ABBREVIATIONS 1

CHAPTER 1: INTRODUCTION 1

1.1. Basic Concepts 2

1.1.1. Induction Machine Operating Principles 2

1.1.2. Common Motor Failures 7

1.2. Commonly Used Health Monitoring Schemes 9

1.2.1. Vibration Monitoring 9

1.2.2. Thermal Monitoring 9

1.2.3. Partial Discharge Testing 10

1.2.4. Electrical monitoring 10

1.3. Motor Current Signature Analysis 12

1.3.1. Air-gap Eccentricity 12

1.3.2. Broken Rotor Bars 14

1.3.3. Bearings Damage 14

1.3.4. Unbalanced Load 16

1.4. Using Motor Current Signature Analysis to Monitor Condition of Multiple Motors 16

1.5. Objective 20

1.6. Outline 20

CHAPTER 2: ANALYSIS OF THE PROBLEM AND ITS APPROACH 21

2.1. Challenges in Resolving Two Signals with Nearly Identical Frequencies 21

2.2. Resolving Two Nearby Signals with No Fundamental Component 22

2.3. Resolving Two Nearby Signals with Fundamental Component 28

2.3.1. Zoom FFT 28

2.3.2. Synchronous Detection 29

CHAPTER 3: SIGNAL PARAMETER ESTIMATION 31

3.1. Preprocessor 32

3.2. Detection algorithm 33

3.3. Selection Algorithm 35

CHAPTER 4: EXPERIMENTAL RESULTS 39

4.1. Experimental Setup 39

4.2. Initial Motor Results 44

4.2.1. 50W Load Condition Results 48

4.2.2. 70W Load Condition Results 51

4.2.3. 120W Load Condition Results 54

4.3. Faulted Motor Results 60

CHAPTER 5: CONCLUSION 65

REFERENCES 66

APPENDIX A: MATLAB CODE OF PROPOSED ALGORITHM 69

LIST OF FIGURES

FIGURE 1.1: Per-phase equivalent circuit for a polyphase induction motor [3] 2

FIGURE 1.2: Torque Speed Curve of an Induction Motor 5

FIGURE 1.3: Example of motor nameplate values. Note that both motors have the same rated speed despite their different sizes. 7

FIGURE 1.4: Common motor failures as a percentage of overall amount of failures showing statistics from first of two surveys conducted by IEEE-IAS and EPRI 8

FIGURE 1.5: Roller bearing diagram showing the critical dimensions for the single-point failures. Note that the ball contact frequency is, where θ is the angle between the centerline of the bearing and F_B, indicates the direction of the force exerted by the ball on the outer race [4]. 15

FIGURE 1.6: Two identical sets of motors 17

FIGURE 1.7: Power vs. speed curve for the motor 19

FIGURE 1.8: Zoomed-in values of power vs. speed curve for the motor 19

FIGURE 2.1: DTFT of agrregate signal 23

FIGURE 2.2: Sampling and windowing for finite duration 23

FIGURE 2.3: DFT of rectangular window 24

FIGURE 2.4: DFT of Hann Window of 1 minute length 25

FIGURE 2.5: DFT of $V[k]$ having 4 minute window length with 0.001 Hz/line resolution 25

FIGURE 2.6: DFT of $V[k]$ having 6 minute window length with 0.001 Hz/line resolution 26

FIGURE 2.7: DFT of $V[k]$ having 8 minute window length with 0.001 Hz/line resolution 26

FIGURE 2.8: DFT of $V[k]$ having 8 minute window length with 0.0001 Hz/line resolution 27

FIGURE 2.9: Zoom FFT principle 29

FIGURE 2.10: Synchronous Detection 30

FIGURE 3.1: Block Diagram of Algorithm 31

FIGURE 4.1: Block Diagram of experiment setup 39

FIGURE 4.2: Circuit Diagram of experiment setup 40

FIGURE 4.3: Power Supply to the Motors 40

FIGURE 4.4: Three phase switches 41

FIGURE 4.5: Motor 1 coupled to dyanamometer 41

FIGURE 4.6: Dyanamometer Controller 42

FIGURE 4.7: Motor 2 coupled to external load 42

FIGURE 4.8: Current and Voltage transducers used in the experiment and their specifications 43

FIGURE 4.9: Main data acquisition board 43

FIGURE 4.10: Rotor eccentricity frequency of individual motors. 47

FIGURE 4.11: FFT of Current from main CTm 49

FIGURE 4.12: FFT of data from CT1 after rotor frequency of motor 1 has been subtracted. 50

FIGURE 4.13: Results of Zoom FFT algorithm where f_{c1} is rotor frequency of motor 1 and f_{c2} of motor 2, ph_1 and mag_1 is phase and magnitude of motor 1 used to form time domain signal to subtract from CT1 data. 50

FIGURE 4.14: 1 minute v/s 2 minute data length for 70W load 52

FIGURE 4.15: FFT of data from CT1 after rotor frequency of motor 1 has been subtracted. 53

FIGURE 4.16: Results of Proposed tracking algorithm where f_{c1} is rotor frequency of motor 1 and f_{c2} of motor 2 54

FIGURE 4.17: Rotor frequency of individual motors. 55

FIGURE 4.18: DFT of subtracted signal for 120W load of 1 minute data length 56

FIGURE 4.19: Results of tracking algorithm for 120W load where f_{c1} is rotor frequency of motor 1 and f_{c2} of motor 2. Here, f_{c2} should be 29.931 56

FIGURE 4.20: DFT of CTm at 120W load for 2 minute 57

FIGURE 4.21: DFT of signal after Motor 1 rotor eccentricity signal has been subtracted 58

FIGURE 4.22: Output of tracking algorithm where f_{c1} is rotor eccentricity frequency of Motor 1 and f_{c2} of Motor 2 58

FIGURE 4.23: Induced fault in Motor 2 61

FIGURE 4.24: DFT of aggregate current for 50W load on Motor 1 and 120W constant load on Motor 2 62

FIGURE 4.25: DFT of aggregate current for 50W load on Motor 1 and 120W faulted load on Motor 2 62

FIGURE 4.26: Motor 2 rotor eccentricity amplitudes 63

FIGURE 4.27: Fault induced Motor 2 rotor eccentricity amplitudes 64

LIST OF TABLES

TABLE 1.1: Key induction-motor circuit parameters 3

TABLE 1.2: Important frequencies and speeds associated with induction machines 4

TABLE 1.3: Common motor failures by percentage 8

TABLE 1.4: Parameters for an example 3-phase, 8-pole machine 18

TABLE 4.1: Power and Torque Values of Motor 1 45

TABLE 4.2: Motor number and their corresponding CT 46

TABLE 4.3: Eccentricity frequency of individual motors for 50W load 48

TABLE 4.4: Eccentricity frequency of individual motors for 70W load 51

TABLE 4.5: Eccentricity frequency of individual motors for 120W load 54

TABLE 4.6: Eccentricity frequency of individual motors for 120W load run for 2 minutes 57

TABLE 4.7: Results of experiment with 1 min data 59

TABLE 4.8: Results of experiment with 2 min data 60

CHAPTER 1: INTRODUCTION

By monitoring the health of induction motors in near real-time, many organizations expect to be able to reduce costs, extend asset lifetime and reduce overall power consumption. To give a sense of the importance of health monitoring, consider that there are an estimated 700 million motors across industrialized nations [5]. The lost lifetime resulting from voltage distortion and imbalance alone is estimated to be about 1 to 2 billion dollars per year [6]. To prevent or at least control such losses, many different health-monitoring methods have been developed over time. Most of these methods, however, are very costly to implement. A 2013 report by NRG Systems [7], for instance, noted that the total cost of a vibration-based monitoring system for a typical wind turbine was about 7000$. For many small electric utilities and other organizations, these costs can be prohibitive, especially because there is no guarantee that the monitoring equipment will actually detect a major fault. One method that has been developed to help reduce costs is motor current signature analysis (MCSA).

The primary concept behind this technique is the notion that tiny signals contained in the stator current provide some indication of motor health. This technique tends to be somewhat less costly since it allows one to detect multiple different faults using only a single sensor. This thesis examines the possibility of expanding this effort even further by monitoring the health of multiple motors using only a single current sensor measuring the aggregate current drawn at a motor control center (MCC) or other similar location. Although such an approach cannot provide the highest level of resolution, it can provide a low-cost means to detect the existence of faults. Dedicated, short-term monitoring equipment can always be added to provide more information.

This chapter introduces the basic concept and necessary background for this thesis.

The first section reviews some basic induction motor properties and describes some of the most common motor failures. Section 1.2 then discusses some of the most common methods for monitoring motor health and explains why many of these methods are cost prohibitive or useful only for off-line testing. Section 1.3 provides more detailed information about motor-current signature analysis (MCSA), which is the primary mechanism upon which the proposed monitoring technique is based. Section 1.4 describes the multi-machine monitoring approach examined in this thesis, and finally Section 1.5 presents a summary of the complete thesis document.

1.1 Basic Concepts

To describe the critical elements of this thesis, it is important to review some basic principles. This section first presents some physical concepts about induction machine operation. It then describes some of the critical motor failures as means to introduce the reader to the types of faults that concern motor operators. More detailed information can be found in various references [3].

1.1.1 Induction Machine Operating Principles

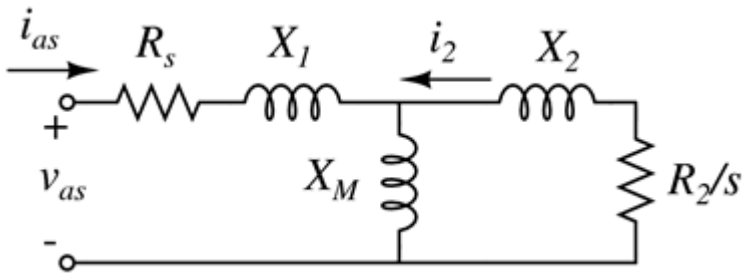

Figure 1.1: Per-phase equivalent circuit for a polyphase induction motor [3]

Figure 1.1 shows the equivalent steady-state circuit model for the three-phase, p-pole induction motor and table 1.1 defines the relevant circuit parameters [3].

Table 1.1: Key induction-motor circuit parameters

Notation	Description
R_1	Stator Resistance
R_2	Rotor Resistance
X_1	Stator Leakage Reactance
X_2	Rotor Leakage Reactance
X_M	Magnetizing Reactance

One additional term that needs definition is the quantity s presented. This value can only be understood with more information about induction-machine operation. When a balanced three-phase voltage source having frequency ω_e is applied to the stator terminals of a machine having p magnetic poles, a rotating magnetic field is produced. This field rotates around the air gap at a rate known as the synchronous speed, ω_s. In terms of the frequency of the voltages this speed is:-

$$\omega_s = \omega_e \left(\frac{2}{p}\right) \tag{1.1.1}$$

For example, the stator-side magnetic field in a four-pole induction machine excited with 60 Hz (120π rad/sec) voltages rotates at 30 Hz (60π rad/sec). When mechanically loaded, this rotating field induces a current in the rotor and forces it to move at a physical speed ω_r. The rotor current consequently creates its own rotating magnetic field that moves about the air gap at the same rate. The resulting torque depends upon the fractional difference between the speeds of these two rotating fields. This quantity is termed slip and is defined as:-

$$s = \frac{\omega_s - \omega_r}{\omega_s} \tag{1.1.2}$$

Note that the rotor-side resistance in Figure 1.1 is inversely proportional to this value.

As shown in [3], this resultant torque is:-

$$T = \frac{3|I_2|^2 R_2}{s\omega_s} \tag{1.1.3}$$

Where I_2 is the magnitude of the current flowing through the rotor-side components shown in Figure 1.1. Further details and complete derivations are beyond the scope of this work. The interested reader is directed to [3]. Table 1.2 summaries the notation associated with the critical frequencies used in this section. The remainder of this document uses this notation.

Table 1.2: Important frequencies and speeds associated with induction machines [3]

Name of Frequency or Speed	Variable Name (rad/sec)	Variable Name (Hz)
Electrical Frequency	ω_e	f_e
Synchronous speed	ω_s	f_s
Rotor mechanical speed	ω_r	f_r
Slip	s	s

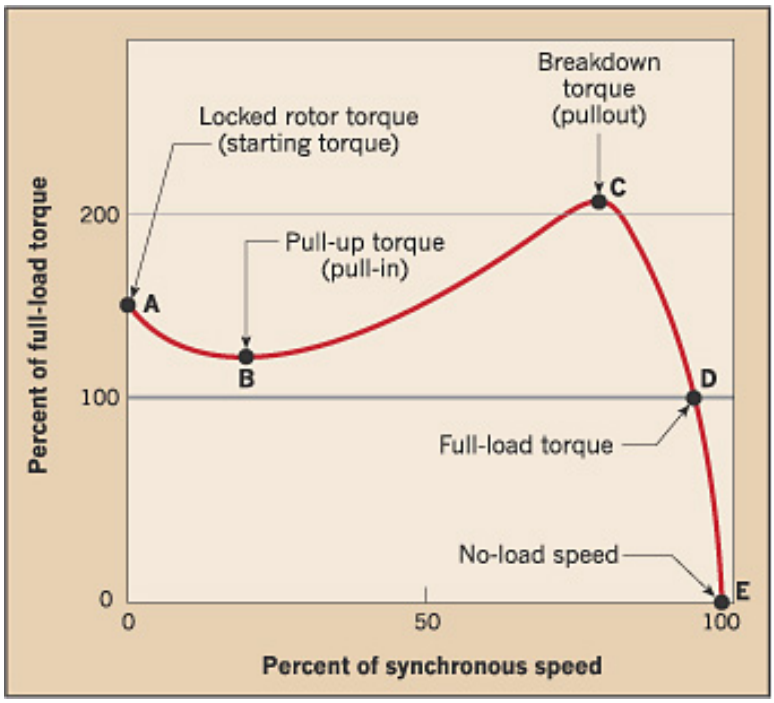

Figure 1.2: Torque Speed Curve of an Induction Motor

Equation 1.1.3 describes the motor's capability to produce a given torque at a given speed. This capability is expressed as a torque-speed curve. Figure 1.2 presents a typical curve. As is common in the industry, this graph is shown in per-unit form, with the torque presented as a percentage of its rated value and the speed given as a percentage of its maximum value (i.e. ω_s). Figure 1.2 defines several important operating points. Instead of describing these in alphabetical order, we discuss them in order of significance as follows:

Operating point A: This is defined as locked-rotor torque and it is the steady-state torque produced by the machine when it is stalled (i.e. at zero speed). At this operating point, the rotor is not moving and the steady-state torque is defined as locked-rotor torque. This is the same as the initial torque produced when an on-line motor is first energized.

Operating point E: When the motor is not loaded (i.e. it does not need to overcome any mechanical resistance), it will rotate at the same speed as the stator flux wave.

This no-load speed is thus ω_s and no torque is produced since no torque is acting to slow the motor down.

Operating point D: This is the rated, or full-load, condition. This is the point near which the machine operates when producing its rated torque. Note that the speed at which rated torque is developed typically occurs at only a few percent slip. For a two-pole motor with a 60Hz electrical frequency, for instance, a rated speed of 58.8 Hz (i.e. 2% slip) would not be uncommon.

Operating point C: This is the maximum torque the machine can produce, and it is typically much larger than the rated value. The machine should pass through this operating point during the transient condition following its initial excitation.

Operating point B: The torque at this operating condition is known as pull-up torque. This operating point is important because if the initial load torque that the motor must overcome is above this value, the machine will not accelerate to its rated speed. For example, if the initial load torque is equal to the pull-up torque, the machine will only accelerate to the speed at which pull-up torque is produced. At this low speed, the machine produces more torque than rated and consumes far more current than its rated value [3].

Significantly more information about these conditions is available in [3] and [8]. The most important fact relevant to this thesis is the notion that most induction motors typically operate between points E and D when in steady-state. As a result, as the mechanical load increases from 0 to 100%, the speed fluctuates only several percent. This fact ultimately means that induction machines with identical pole numbers tend to operate at nearly identical speeds regardless of their size. For example, consider a bus feeding the two motors with the nameplates given in Figure 1.3. Both operate at a speed of 3450 RPM (i.e. 57.5Hz or 5% slip) when providing their respective rated torques. Note, however, that the two machines have drastically different rated

conditions (i.e. 10 HP vs 1.5 HP). This issue is revisited in Section 1.4 when discussing the key concept of this thesis.

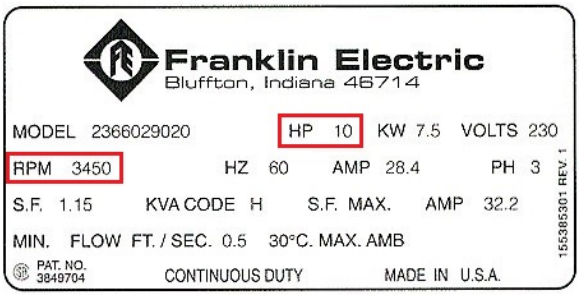

(a) 10 HP, 2-pole motor with speed 3450 RPM

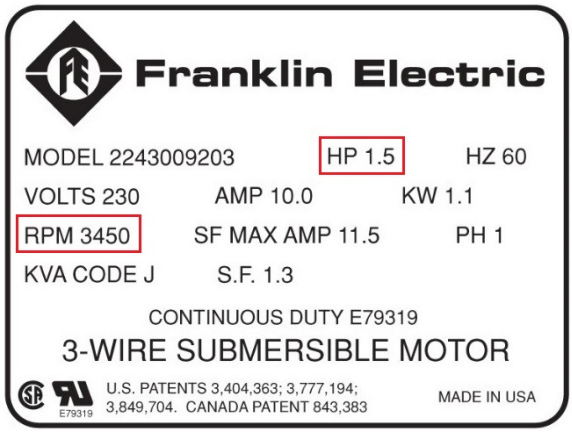

(b) 1.5 HP, 2-pole motor with speed 3450 RPM

Figure 1.3: Example of motor nameplate values. Note that both motors have the same rated speed despite their different sizes.

1.1.2 Common Motor Failures

Several studies have documented the major sources of failure in large induction motors [9] [10] [11] [12] and [13]. Table 1.3 summarizes the results from [11] and [12]. These results list the component that ultimately caused a complete failure. Typically, these faults begin as various mechanical, thermal, and electrical stresses and slowly degrade individual components. In the case of stator-related failures, for instance, the majority are caused by degraded insulation. These sorts of failures often start as small breaks in winding insulation, perhaps caused by vibrations. Over time, they develop into catastrophic failures such as phase-to-ground short circuits. Similarly, most rotor-related faults are caused by faulty squirrel cages, in which individual broken rotor bars lead to completely cracked cages. The most frequently failed components are bearings, which account for nearly 40% of all issues.

Table 1.3: The most common motor failures by percentage. These are taken from two of the most cited studies in the literature

Failed Component	From [11]	From [12]
Bearing	44	41
Stator	26	36
Rotor	8	9
Other	22	14

Several other studies like IEEE-IAS and EPRI have found similar results as illustrated in Figure 1.4. It should be noted that bearing failures typically result in excessive vibrations and other phenomena that can ultimately impact elements such as the stator windings and rotor cage.

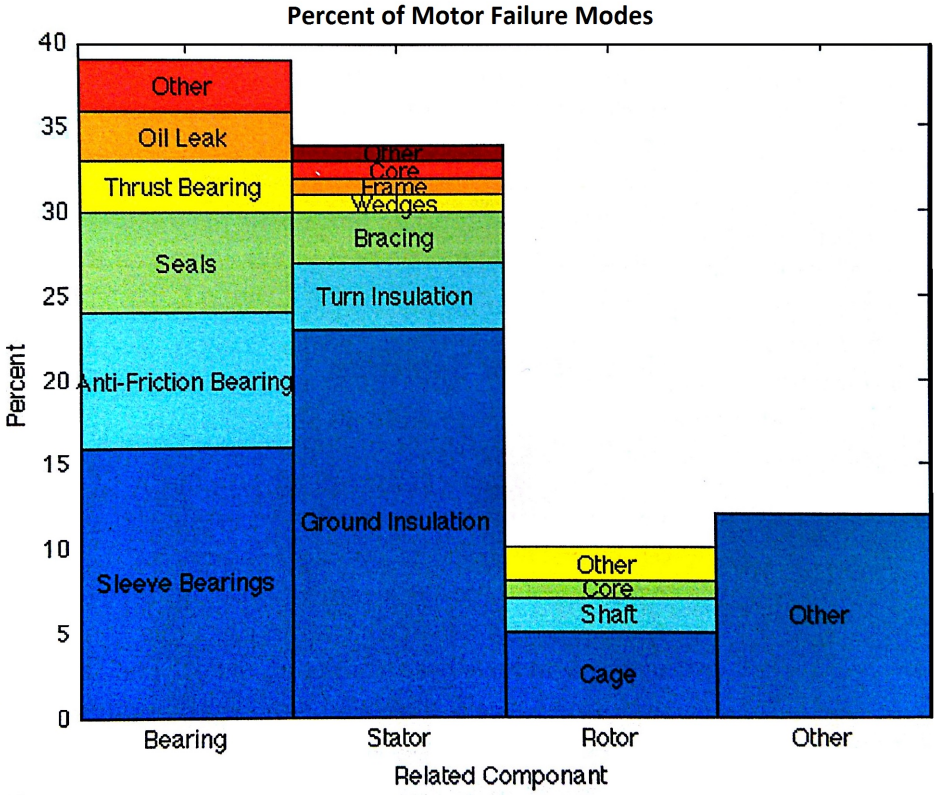

Figure 1.4: Common motor failures as a percentage of overall amount of failures showing statistics from first of two surveys conducted by IEEE-IAS and EPRI

1.2 Commonly Used Health Monitoring Schemes

Multiple methods have been developed to detect motor faults, some of which have been used commercially and others which have only been explored in laboratory environments. This section provides a very brief introduction to some of the most common techniques.

1.2.1 Vibration Monitoring

Vibration signals are commonly used to detect critical motor faults, such as bearing failures, structural resonances, foundational issues, mechanical imbalances, and winding damage. Vibration measurements are provided by accelerometers and proximity probes. These additional sensors and their data-acquisition systems can be very costly, but they are known to provide a high level of detail about the early-stage development of many catastrophic issues, particularly those related to bearings. Because of their cost, they are typically only used in the most critical applications and for the largest motors in major power plants and industrial facilities. Several manufacturers provide both dedicated monitoring solutions as well as handheld instruments that can be used for periodic spot checks [14], [15].

1.2.2 Thermal Monitoring

Thermal monitoring of electric machines can be performed in various ways, including hand-held infrared cameras and on-board installed sensors such as thermocouples or resistance temperature detectors. Thermal measurements can indicate the existence of overheated bearings and windings. Such issues typically arise in the latter stages of a fault and just before a major issue is about to occur. Infrared thermography is commonly used to perform spot checks to detect developing anomalies. Devices such as thermocouples and resistance temperature detectors (RTDs) are embedded into large motors for last-minute protection purposes [16].

1.2.3 Partial Discharge Testing

Some 30 to 40% of all motor failures are caused by faulty stator windings [9] [10] [11] [12] and [13]. These issues typically manifest as phase-to-ground or phase-to-phase shorts, but they begin in more benign ways as winding insulation slowly degrades. Early-stage deterioration often causes turn-to-turn faults, in which two or more turns of a single coil are short-circuited. The current in the shorted turns is substantially higher than the operating current and thus this additional current increases the winding temperature to the point at which more severe damage can occur. This is one of the primary reasons why it is believed that turn-to-turn faults are the original precursor to many more severe issues [17]. Although thermal monitoring can indicate such critical issues, the temperature typically does not increase significantly until the point at which catastrophic failure is imminent. An alternative approach to detect early-stage issues is to use probes that can detect the existence of so-called partial discharges that occur when dielectric breakdown happens between windings. The existence of this discharges is an early indicator of stator insulation failure. These methods have been found useful at voltages above 4kV, and various commercial systems are available. For low voltage motors, no comparable method exists [18].

1.2.4 Electrical monitoring

Electrical monitoring is one of the most attractive methods for real-time analysis because electrical sensors, namely voltage and current transducers, are very easy to install and are essentially required in most large motor applications. The most powerful electrical technique is motor current signature analysis. The sections below describe the traditional approach to MCSA as well as some modified approaches that have been developed over time.

- Traditional MCSA: Various tell-tale signals are known to exist within the stator

current of an electric machine. For instance, various higher order electromagnetic interactions within the motor cause effects such as broken rotor bars to induce small signals within the stator current. Stator current DFT is then used to detect abnormalities of current amplitude at particular frequencies which correspond to faults in the motor. Section 1.2 provides more details on this approach, which has been successfully commercialized by several manufacturers [19].

- Extended Park's Vector Approach (EPVA): Several MCSA-variant methods exist. These methods typically include some additional pre or post-processing approach on the measured current. In the case of EPVA, the terminal voltages and currents are transformed into a rotating reference frame in which the currents and voltages are represented in a complex plane with a direct axis and quadrature axis [20] [21]. The so-called Park's vector will rotate around this plane and trace out a circle when the machine is healthy. If the pattern becomes elliptical, a fault is believed to exist [18]. This approach is found in commercial systems [19].

- Instantaneous Power Signature Analysis (IPSA): This, too, is a variant of traditional MCSA in which the measured voltages and currents are used to develop an instantaneous power signal. This waveform can be examined in the frequency domain and can potentially provide more information about faults than those methods based solely on the current [18].

- Motor Voltage Signature Analysis (MVSA): Stator voltage has also proven to be useful in motor health monitoring, largely because unbalanced or distorted voltages can cause numerous other motor faults such as overheating and uneven rotation (i.e. eccentricity). Several commercially available MCSA systems also monitor voltage as a part of their standard offering [19].

1.3 Motor Current Signature Analysis

MCSA has been discussed in the literature for many years, and several successful commercial products have been developed to utilize it. Essentially, various non-ideal conditions in the machine itself give rise to small signals in the air-gap flux that ultimately result in stator current fluctuations [18]. These signals appear at frequencies related to various machine parameters such as the number of rotor bars or the number of balls in the machine's rolling-element bearings. Typically, the frequency of these signals is related to the rotor speed or to the fundamental frequency of the applied voltage, where rotor speed fluctuates from motor to motor based on its air-gap eccentricity. Rotor speed is given as :

$$f = \frac{120 * Line\, frequency\, (F)}{Number\, of\, poles\, (P)} \tag{1.3.1}$$

Following subsections briefly reviews some of the common faults detected using MCSA such as Air-gap Eccentricity, Broken Rotor Bars and Bearings Damage respectively.

1.3.1 Air-gap Eccentricity

There are two types of air gap eccentricity: static (where the position of minimum radial air-gap length is fixed) and dynamic(where the minimum air gap revolves with the rotor and is a function of space and time). Static air gap eccentricity can be caused by stator core ovality or incorrect positioning of the rotor or stator whereas dynamic eccentricity can be caused by a non-concentric outer rotor diameter, thermal bowing of the rotor, or bearing wear and movement. Static eccentricity causes a steady force called unbalanced magnetic pull (UMP) on the rotor in one direction that tries to pull the rotor even further from the stator bore center in the direction of minimum air-gap. Dynamic eccentricity causes a force (rotating UMP) that rotates at the rotor speed (a rotating force wave). If the levels of air-gap eccentricity are not kept

within specified limits (typically a maximum of 10 percent in three-phase induction motors), then both types of eccentricity can cause excessive stressing of the motor and can increase bearing wear. The radial magnetic force waves also act on the stator core assembly and rotor cage subjecting the stator and rotor windings to potentially harmful vibration. High UMP due to severe air-gap eccentricity can ultimately lead to a rotor to stator rub with consequential damage to the core and stator windings or the rotor cage. This can cause insulation failure of the stator winding or the breaking of rotor cage bars or end rings. Frequencies which get effected due to air gap eccentricity is located at [22]:

$$f_{ec} = f_e \left\{ (R \pm n_d) \left(\frac{1-s}{p} \right) \pm n_{\omega s} \right\} Hz \tag{1.3.2}$$

Where,

f_{ec} = Frequency components that are a function of airgap eccentricity (Hz)

f_e = Supply frequency (Hz)

R = Number of rotor slots

$n_d = \pm$ 1

$n_{\omega s}$ = 1, 3, 5, 7

s = Slip

p = Pole-pairs

With $n_d = 0$ in Equation 1.3.2, this gives the classical rotor slot passing frequency (rotor speed) components. Amplitude of frequency at $n_d = \pm 1$ (actually spaced at $\pm f_r$ i.e rotational speed frequency, around the rotor slotting components) increases with increase in eccentricity [23].

1.3.2 Broken Rotor Bars

The stator winding of a motor produces a forward rotating magnetic field at synchronous speed due to power being fed to it. Any stator winding asymmetries will result in a backward rotating field as well. In reverse logic, the stator winding will be induced with voltage and current when in a similar rotating field. Similarly, the rotor winding of the motor gets induced by the forward rotating field around the rotor, hence it gets induced with voltage and current at slip frequency. When broken rotor bar/s exist in the rotor, they contribute to a magnetic field rotating backward at slip frequency which in turn induce a current and voltage in the stator winding. In 1920, Williamson and Smith mathematically derived the frequencies which get effected when a motor has broken rotor bars as:

$$f_{sb} = f_e(1 \pm 2s)Hz \tag{1.3.3}$$

Where f_{sb} is the side band frequency (twice slip frequency) which increase in magnitude when rotor bars get broken and f_e is the supplied voltage frequency.

1.3.3 Bearings Damage

Forcing a bearing into shaft inappropriately may lead to brinelling (indentation damage caused by impact where metal is displaced usually by the rolling element striking the raceway surface) and false brinelling (rubbing action of metal to metal contact). Since ball bearings support the rotor, any bearing defect will produce a radial motion between the rotor and stator of the machine. The mechanical displacement resulting from damaged bearing causes the machine air gap to vary in a manner that can be described by a combination of rotating eccentricities moving in both directions. These defects produce vibrations at distinct frequencies. Depending upon the location of the defect, these are known as the cage fault frequency (f_{CF}), the ball-pass inner raceway fault frequency (f_{IRF}), the ball-pass outer raceway fault

frequency (f_{ORF}), and the ball fault rotational frequency (f_{BF}). As derived in [24], the vibration signals generated at these frequencies depend upon various machine and bearing parameters. These frequencies are

$$f_{CF} = \frac{1}{2} f_r (1 - \frac{D_B cos\theta}{D_p}) \tag{1.3.4}$$

$$f_{ORF} = \frac{N_B}{2} f_r (1 - \frac{D_B cos\theta}{D_p}) \tag{1.3.5}$$

$$f_{IRF} = \frac{N_B}{2} f_r (1 + \frac{D_B cos\theta}{D_p}) \tag{1.3.6}$$

and

$$f_{BF} = \frac{D_p}{2d_B} f_r (1 - \frac{D_B^2 cos^2\theta}{D_p^2}) \tag{1.3.7}$$

In these equations,f_r is the mechanical speed of the rotor,N_B is the number of balls, D_B is the ball diameter, D_p is the ball pitch diameter, and θ is the ball contact angle. Figure 1.6 provides a diagram defining these geometric constants.

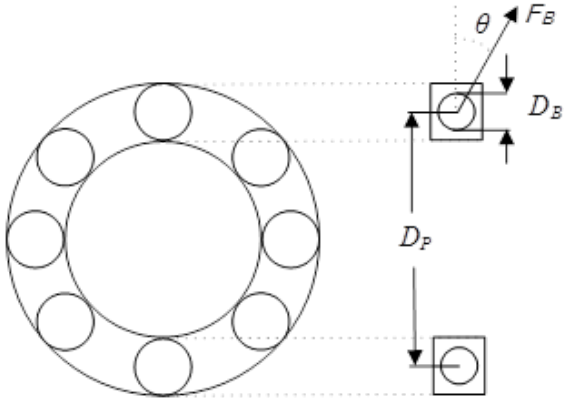

Figure 1.5: Roller bearing diagram showing the critical dimensions for the single-point failures. Note that the ball contact frequency is, where θ is the angle between the centerline of the bearing and F_B, indicates the direction of the force exerted by the ball on the outer race [4].

Any vibrations occurring at these frequencies are transmitted through the bearing

housing and may appear in the stator current. Such signals can appear as amplitude modulated signals in the current, in which case they occur at the frequencies:

$$f_{BE} = |f_s \pm m f_v| \tag{1.3.8}$$

where f_s is the frequency of the stator voltage, m is an integer, and f_v is one of the characteristic fault frequencies defined above [25] [26].

1.3.4 Unbalanced Load

When an electrical load is unbalanced it results in variation in the torque required to overcome the weighted portion of the load. This leads to rotor speed fluctuation which manifests as harmonics in stator current due to induction of stator windings. The stator current already has a line frequency component which is present from the non-varying speed component of the rotor. The other terms are symmetric sidebands which arise from the shaft speed variation. These shaft speed oscillation harmonics are expressed by :

$$f_{sso} = f\left[k\left(\frac{1-s}{p}\right) \pm 1\right] Hz \tag{1.3.9}$$

where s is per unit slip, k=0,1,2.. and p is the number of pole pairs [27].

1.4 Using Motor Current Signature Analysis to Monitor Condition of Multiple Motors

Although effective methods clearly exist for monitoring the health of individual induction machines, the cost associated with such systems is high enough such that many utilities cannot afford to deploy them. This thesis examines an alternative approach such as the one shown in Figure 1.6. In this approach, a single set of current transducers measures the aggregate current flowing to a bank of motors fed from a motor control center (MCC). For the sake of redundant design, these MCCs typically feature at least two motors used in the same application. For example,

motors 1A and 1B in Figure 1.6 might represent two fan motors and motors 2A and 2B might represent two pump motors. Consider a simple case with two sets of near identical motors.

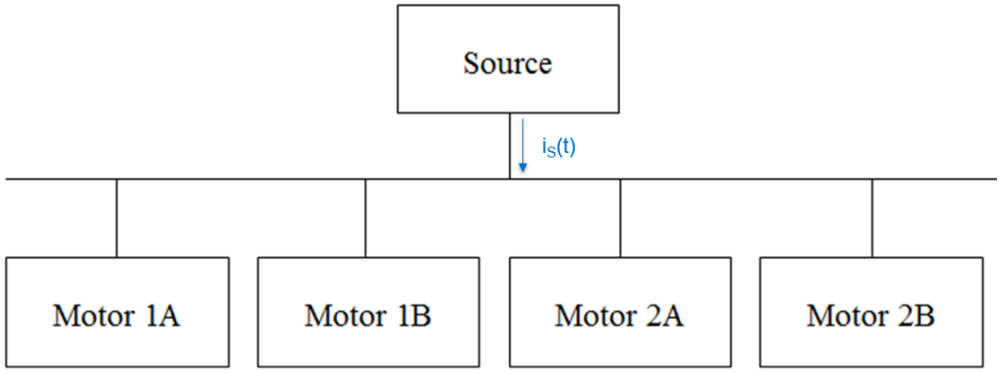

Figure 1.6: Two identical sets of motors

Imagine that only Motor 1A and Motor 1B are operating. If the source is balanced and not distorted, the aggregate current in phase A might be of the form:

$$i_S(t) = I_{1A}\cos(\omega_e t + \phi_{1A}) + I_{1B}\cos(\omega_e t + \phi_{1B}) + i_{health}(t). \tag{1.4.1}$$

The first two terms represent the fundamental load current drawn by each motor. The latter term, referred to as $i_{health}(t)$, represents non-fundamental, health-related signals such as the ones described in the previous section. These signals could be caused by any number of phenomena, and most likely any functional motor would contain multiple such signals. In this context, we can think of each motor as a set of parallel-connected current sources, each drawing a current related to its individual fault. Given that these sources are in parallel, we can use superposition to examine each separately. For illustrative purposes, let's consider that both machines have some slight amount of static and dynamic eccentricity [18]. As a result, both will draw currents having frequencies related to the rotational speed, i.e

$$f_1 = |f_e \pm k f_r| \tag{1.4.2}$$

where k=1,2,3,...

Now, Considering only k=1, $i_{health}(t)$ might be of the form:

$$i_{health}(t) = I_{h,1A}\cos((\omega_e + \omega_{r,1A})t) + I_{h,1B}\cos((\omega_e + \omega_{r,1B})t). \tag{1.4.3}$$

where $\omega_{r,1A}$ and $\omega_{r,1B}$ are the respective rotational speeds of the two motors and the amplitudes $I_{h,1A}$ and $I_{h,1B}$ are harmonics and several orders of magnitude smaller than the magnitude of the fundamental currents I_{1A} and I_{1B}.

In a traditional MCSA application, a technique such as the Discrete Fourier Transform (DFT) would be applied to analyze the individual currents flowing to each motor. The goal would be to track the amplitudes $I_{h,1A}$ and $I_{h,1B}$. Growing amplitudes would suggest that the rotation is becoming more eccentric. In this problem, our goal is to track the same two amplitudes using a single CT measuring the complete current $i_S(t)$. Given that the two motors are employed for the same application, it is reasonable to expect that they might operate at nearly the same load. As an example, consider the 4160V, 1000kW motor with the parameters provided in Table 1.4.

Table 1.4: Parameters for an example 3-phase, 4160V, 60Hz, 1000kW, 8-pole machine [3]

Parameter	Value
R_1	0.220Ω
R_2	0.207Ω
X_1	1.95Ω
X_2	2.42Ω
X_M	45.7Ω

Consider two of these machines operating in parallel, with one providing rated power and the other providing 90% of rated power (900kW). Figure 1.7 shows the mechanical output power of this machine as a function of speed. Note how steep the

curve becomes near the rated operating point. As shown in the zoomed version in Figure 1.8, a 10% difference in output power represents less than a 2RPM change in speed. Despite a 100kW difference in power, the speed difference is small enough that the health signals mentioned above are separated only by 0.033Hz or 0.2094rad/sec.

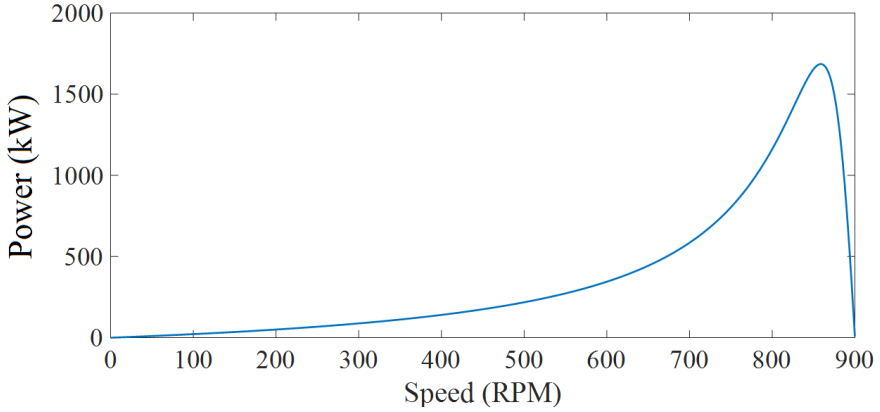

Figure 1.7: Power vs. speed curve for the motor with the parameters provided in Table 1.4

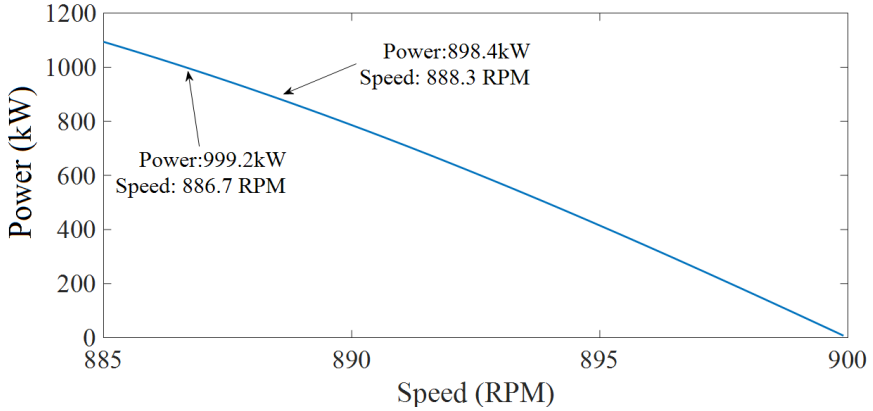

Figure 1.8: Zoomed-in values of power vs. speed curve for the motor with the parameters provided in Table 1.4

This example helps to frame the challenges associated with this project. Specifically, the two signals in Eq.1.4.3 need to be individually resolved even though they may be separated by less than 0.01Hz. The DFT can theoretically detect such close frequencies, but there are several practical challenges that must be addressed. These issues are explored more explicitly in the next chapter.

In addition to potential signal-processing challenges, it is unlikely that any motor remains at a constant speed for any appreciable amount of time. Voltage fluctuations, parameter dependence upon temperature, and short-term load variations can easily cause speeds to change by more than the difference noted here [8]. Given that so many health-related signals depend upon motor speed, this issue must be thoroughly addressed. The processes for tracking such small differences in frequency are the primary topic of this work.

1.5 Objective

The objective of this thesis is to explore techniques that will make it possible to address the issues pertaining to speed related faults in induction motors.

1.6 Outline

This chapter has shown that many of the signals essential for MCSA, whether they be for detecting eccentricity, broken rotor bars, or faulty bearings, depend upon motor speed. In addition, it has demonstrated that two different motors connected to the same bus can easily have nearly the same speed and that these speeds can easily fluctuate over time. Since so many of the signals necessary for MCSA depend upon speed, these issues must be addressed. Chapter 2 analyzes the inherent signal processing challenges associated with tracking these frequencies. Chapter 3 then describes the measurement process developed to overcome these challenges. Chapter 4 then presents experimental results demonstrating that this approach can detect small signals generated by two similar motors operating at nearly identical speeds. Finally, Chapter 5 presents conclusions and directions for future research.

CHAPTER 2: ANALYSIS OF THE PROBLEM AND ITS APPROACH

The previous chapter noted the difficulty in monitoring the behavior of multiple motors using only measurements of aggregate current. This chapter closely examines the technical challenges by considering some explicit examples. The first section examines the difficulty inherent in utilizing the Fourier transform to monitor the health of two motors that operate at nearly similar speeds. Section 2.2 considers the challenge of distinguishing between two signals with frequencies that are very close in value without the fundamental frequency in the signal. Section 2.3 discusses a methodology that can be used to help distinguish such nearby frequencies.

2.1 Challenges in Resolving Two Signals with Nearly Identical Frequencies

Equation 2.1.1 provides an example of current waveform that might be drawn by two motors connected in parallel operating at nearly same speed. The two individual load currents could be combined into one sinusoid to yield a total current of the form

$$i_S(t) = I_1 \cos(\omega_e t + \phi_1) + i_{health}(t) \tag{2.1.1}$$

If we again focus on the eccentricity-related harmonics discussed previously, we can view $i_{health}(t)$ to be of the form given in Equation 1.4.3. This yields a total current of the form

$$i_S(t) = I_1 \cos(\omega_e t+\phi_1)+I_{h,1A} \cos((\omega_e+\omega_{r,1A})t)+I_{h,1B} \cos((\omega_e+\omega_{r,1B})t)+i_X(t) \tag{2.1.2}$$

The term $i_X(t)$ represents all other signals that might appear in the current waveform, such as those related to broken rotor bars or bearings. In this case, we focus

specifically on the main load current (i.e. the component with frequency ω_e) and the eccentricity-related signals with frequencies $(\omega_e + \omega_{r,1A})$ and $(\omega_e + \omega_{r,1B})$. As noted in Chapter 2, there are two key challenges:

- Challenge 1: $I_1 \gg I_{h,1A}, I_{h,1B}$
- Challenge 2: $\omega_{r,1A} \approx \omega_{r,1B}$

To understand the impact of these issues, we will separately examine how they impose constraints upon the use of the Discrete Fourier Transform, which is the typical analytical tool for MCSA. We first consider the case in which the fundamental frequency component has been removed from the overall waveform and we must simply resolve two nearby signals. We then consider the case in which the fundamental frequency remains as a part of the signal.

2.2 Resolving Two Nearby Signals with No Fundamental Component

We begin by considering a general signal of the form

$$x(t) = A_0 \cos(\omega_{A0} t + \phi_0) + A_1 \cos(\omega_{A1} t + \phi_1) \tag{2.2.1}$$

with $\omega_{A0} \approx \omega_{A1}$ and $A_0 \approx A_1$. Assuming ideal sampling with no quantization error, the corresponding discrete-time signal will be as follows:

$$x[n] = A_0 \cos(\omega_{D0} n + \phi_0) + A_1 \cos(\omega_{D1} n + \phi_1) \tag{2.2.2}$$

Where, if we sample at frequency $f_s = 1/T_s$, the corresponding discrete time frequencies are:

$$\omega_0 = \omega_{A0} T_s \tag{2.2.3}$$

and

$$\omega_1 = \omega_{A1} T_s \tag{2.2.4}$$

respectively. Note discrete-time frequencies vary cyclically from $-\pi$ to π. When $x[n]$ has the form shown in Eq.2.2.2, the corresponding Discrete Time Fourier Transform (DTFT) will appear as shown in Figure 2.1. Note that the DTFT has distinct impulses at the frequencies $\pm\omega_0$ and $\pm\omega_1$. Note also that the DTFT is periodic with frequency 2π, so similar impulses would be located at frequencies $\omega = 2n\pi \pm \omega_0$ for all integer values of n [28].

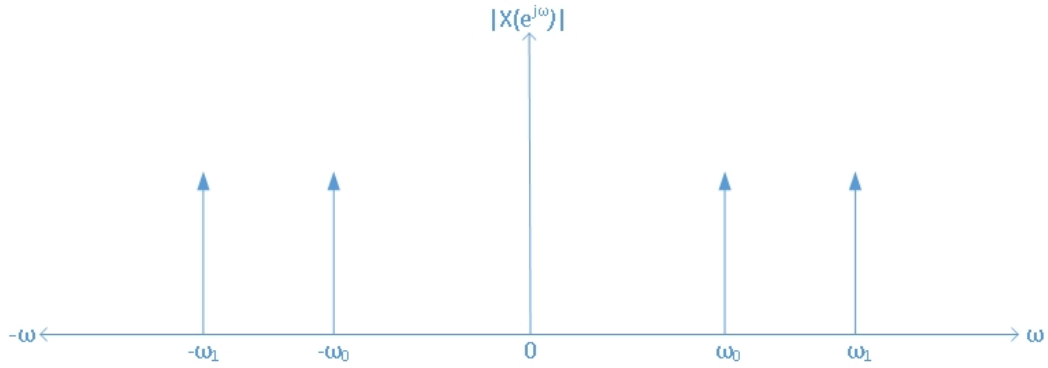

Figure 2.1: DTFT of agrregate signal

Figure 2.2: Sampling $x[n]$ for only a finite time window can be viewed as modulation by a finite-duration window function $w[n]$

Figure 2.1 shows the DTFT of $x[n]$, which includes two signals that theoretically have infinite support (i.e. they are defined for $-\infty < n < \infty$). In reality, one only measures the signal $x(t)$ for a finite time and as a result the measured discrete-time signal has only finite support. Figure 2.2 shows one way to view this finite sampling window. If we measure only L samples of the sequence $x[n]$, then we can view this as modulating $x[n]$ by an L-point sequence $w[n]$. The resulting signal is:-

$$v[n] = x[n]w[n] = A_0 w[n]cos(\omega_0 n + \phi_0) + A_1 w[n]cos(\omega_1 n + \phi_1) \tag{2.2.5}$$

This windowed signal is 0 outside the window from n=0 to n=L-1. When taking the DTFT of $v[n]$, we note that we are taking the transform of the product of two signals. By definition, the DTFT of $x_1[n]x_2[n]$ is $X_1(e^{j\omega}) * X_2(e^{j\omega})$. When taking the DTFT of Eq. 2.2.5, we note that the DTFT of two modulated signals is their convolution in frequency domain.

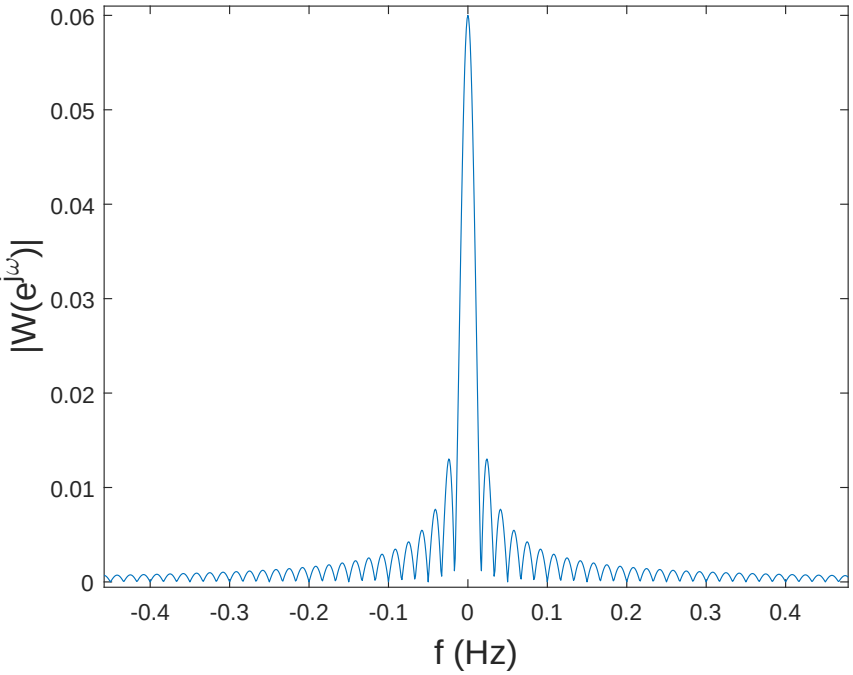

Figure 2.3: DFT of rectangular window of 1 minute length

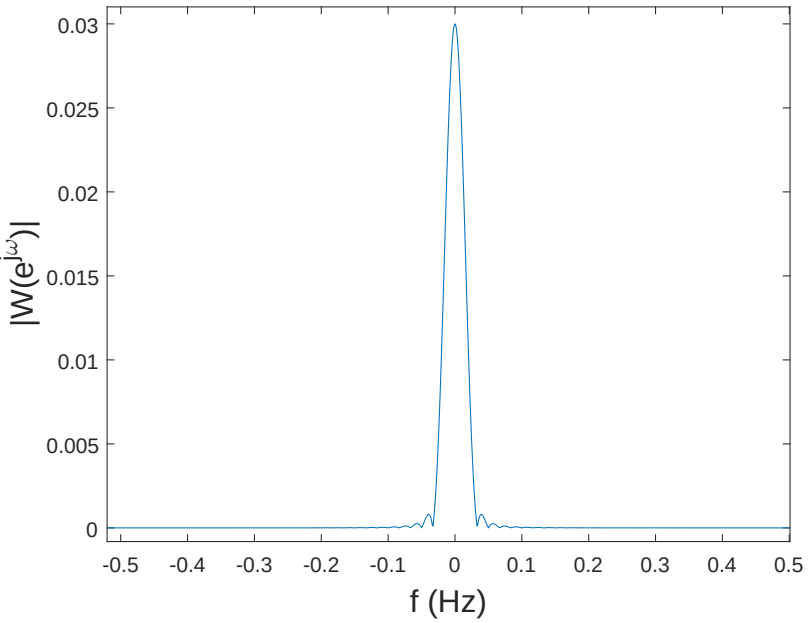

Figure 2.4: DFT of Hann Window of 1 minute length

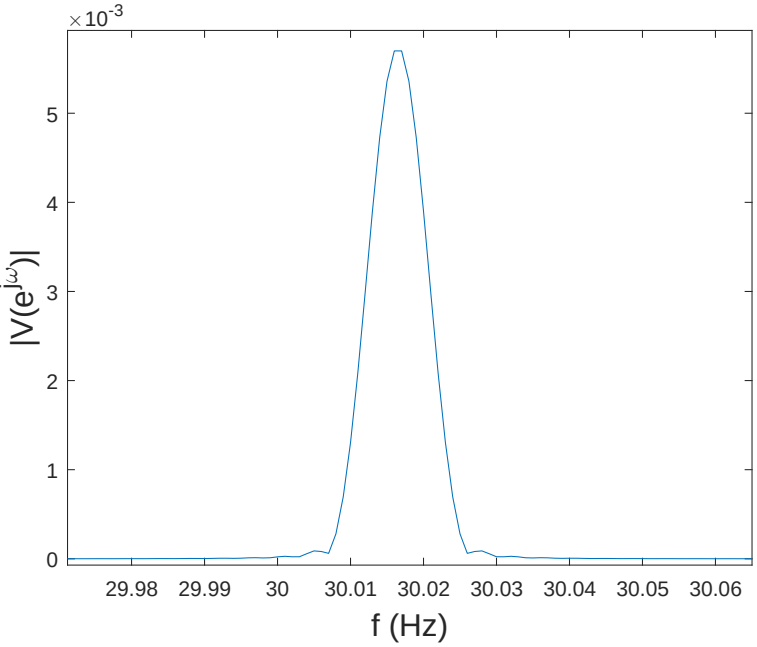

Figure 2.5: DFT of $V[k]$ having 4 minute window length with 0.001 Hz/line resolution

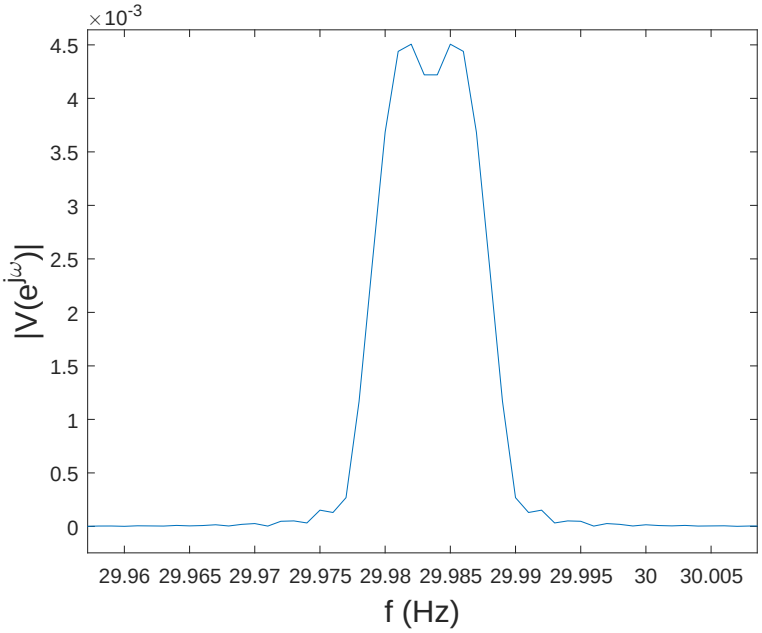

Figure 2.6: DFT of $V[k]$ having 6 minute window length with 0.001 Hz/line resolution

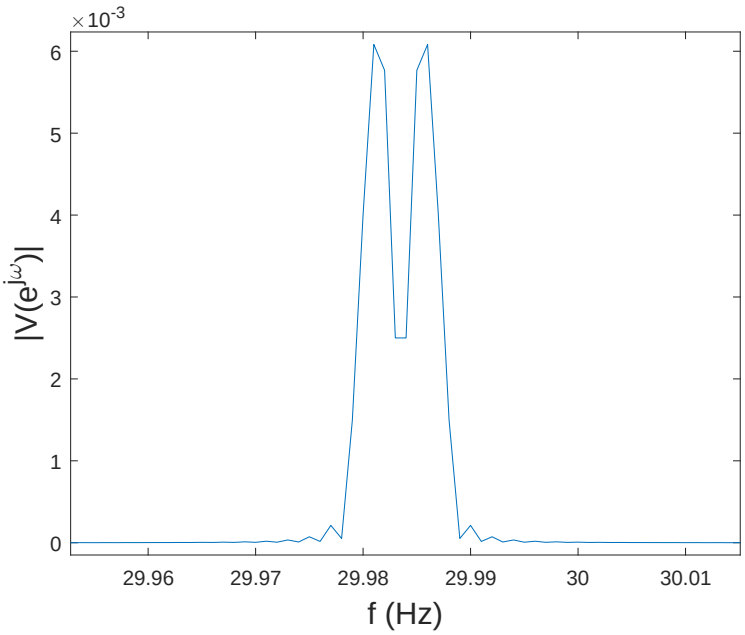

Figure 2.7: DFT of $V[k]$ having 8 minute window length with 0.001 Hz/line resolution

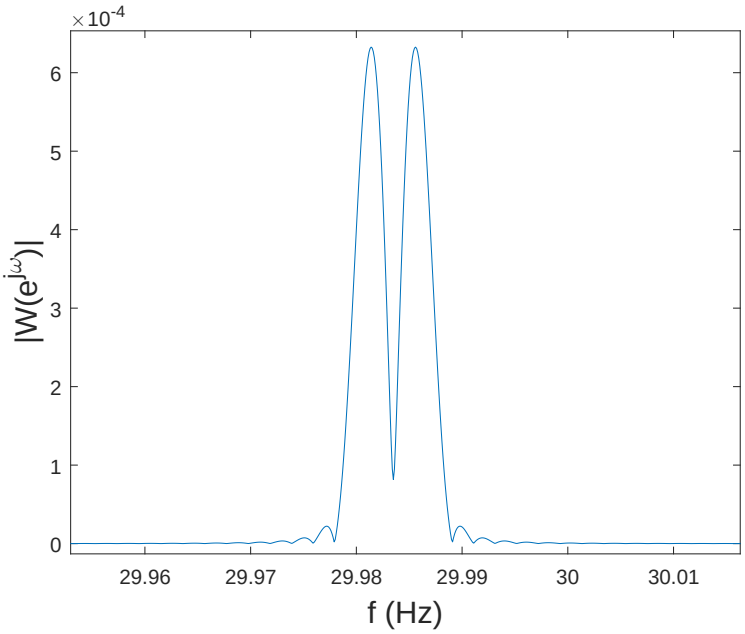

Figure 2.8: DFT of $V[k]$ having 8 minute window length with 0.0001 Hz/line resolution

Figures 2.5 to 2.8 illustrates the importance of frequency resolution and signal length when two frequencies which are extremely close need to be distinguished. Frequency resolution is the distance between two adjacent data points in the DFT. However, by taking FFT over an increased number of bins, a resolution increase simply takes more number of discrete samples than the length of the data i.e frequency axis will span more values, they will be spaced less distance from each other while keeping the same sampling frequency. Hence the resolution of the transform is increased without an increase of actual sampling rate. Resolution can also be increased by increasing the signal length (lower value of resolution indicates the distance between two bins is smaller) as is evident from Equation 2.18. It is well established that only spectral components separated by a frequency larger than the frequency resolution will be resolved. Frequency resolution and signal length correspond as:

$$Resolution = \frac{Sampling\ Frequency\ (F_s)}{Length\ of\ signal(N)} \tag{2.2.6}$$

2.3 Resolving Two Nearby Signals with Fundamental Component

This thesis approaches the problem of having two signals very close to each other with the fundamental component present in the aggregate signal in two steps:-

1. Zoom FFT of fundamental component and its harmonics (section 2.2.1)

2. Synchronous Detection of the nearby signals (section 2.2.2)

When the current signal consisting of nearby signals of interest and fundamental component is fourier transformed by DFT in low sampling rate, the nearby signals cannot be resolved. They appear as Figure 2.5, meshed together. Figure 2.5 had a 4 minute signal length with 0.001 Hz/line resolution and 120 Hz sampling rate, effectively having 480,000 (4*120*1/0.001) data points (DFT bins). When this resolution is increased both by line resolution of 0.0001 Hz/line and signal length of 8 minute, number of DFT bins increases to huge value of 9,600,000. However we do not really need the resolution of the entire signal to be increased as our two nearby points being rotor eccentricity frequency of the two motors lie around the first fundamental frequency harmonic. Hence a very selective resolution increase has to be performed to limit the data required. This procedure is performed by Zoom FFT algorithm (used by the preprocessor algorithm in this thesis) which is explained further in Section 3.1.

After Zoom FFT is performed to extract signals at fundamental frequency and its harmonics, synchronous detection technique is employed to extract the two nearby frequencies. Synchronous detection is explained in section 3.2.

2.3.1 Zoom FFT

The two nearby frequencies corresponds to rotor eccentricity frequencies of Motor 1 and Motor 2 and the fundamental component corresponds to line frequency of 60 Hz. Consider the following Figure 2.9:

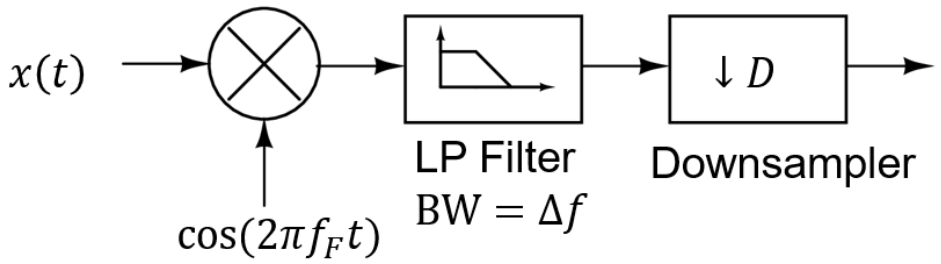

Figure 2.9: Zoom FFT principle

Here, $x(t)$ is the current signal which comprises of fundamental frequency and two nearby frequency

$$x(t) = A\cos(2\pi f_F t) + A_1\cos(2\pi f_1 t) + A_2\cos(2\pi f_2 t) \tag{2.3.1}$$

where, f_F is the fundamental frequency, A, A_1 and A_2 are amplitudes of fundamental and two nearby signals respectively having f_1 and f_2 frequencies near first harmonics of f_F. Multiplication of $x(t)$ shifts area around f_F to baseband. Then a low-pass filter is applied to extract a small band near the base of width Δf. This process can be done is various ways, the most obvious one being having a bandpass filter around fundamental frequency f_F of width Δf. Next, the signal is downsampled so higher frequencies are not represented. This procedure gives a narrow band of frequencies whose resolution can then be increased without overhead of large data length. Zoom FFT concept is further explored in section 3.1 as preprocessor used in this thesis.

2.3.2 Synchronous Detection

After Zoom FFT provides a higher resolution around the desired band of frequencies, the nearby frequencies are then determined using synchronous detection and frequency mixer principle as shown in figure 2.10:

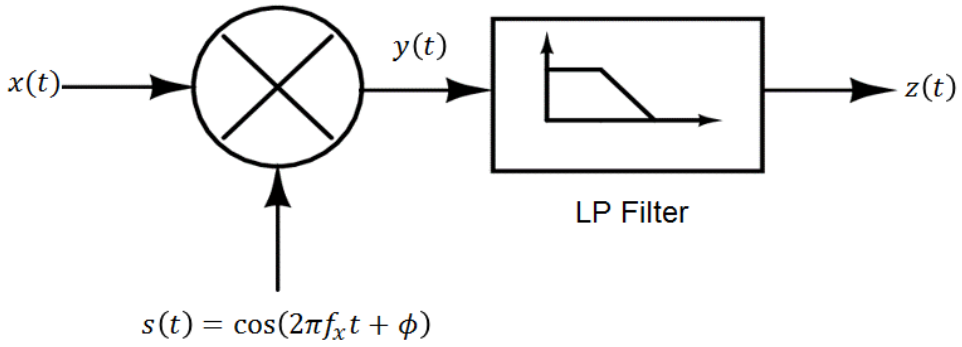

Figure 2.10: Synchronous Detection

To find one of the frequencies of nearby signals (for example f_1 from Eq. 2.2.1), $x(t)$ is multiplied like in the previous section 2.2.1. However instead of multiplying with a sinusoid at fundamental frequency, it is instead multiplied with a range of frequency f_x till one of them equal f_1. The signals then multiply using the following trigonometry identity:-

$$cos^2 A = \frac{1 + cos2\omega_A}{2}$$

Hence at $f_x = f_1$,

$$y(t) = A_1 \cos\omega_A * \cos(2\pi f_1 t) = A_1 cos^2\omega_A = \frac{A_1(1 + cos2\omega_A)}{2} = \frac{A_1}{2} + \frac{A_1 cos2\omega_A}{2}$$

where $\omega_A = (2\pi f_1 t)$.

The low-pass filter then effectively blocks the higher frequency content at $\cos 2\omega_A$ leaving half the signal amplitude $A_1/2$ resulting from the mixer or multiplication. When a range of frequencies are looped through and multiplied, the only frequency which gives this half amplitude result is the frequency which matches that of the nearby signal (A) and then can be identified. This signal detection and selection is elaborated in section 3.2 and 3.3. Once frequency is established, phase ϕ can be detected using the same principle by keeping the selected frequency and looping through a range of phase vales.

CHAPTER 3: SIGNAL PARAMETER ESTIMATION

Accurate procurement of data needed for this (and any) experiment is vital to its success. As extremely low frequency signals were needed to be measured, it was essential that the data was preprocessed to zoom in on these signals with low magnitude. The following flow chart explains how this process was done:-

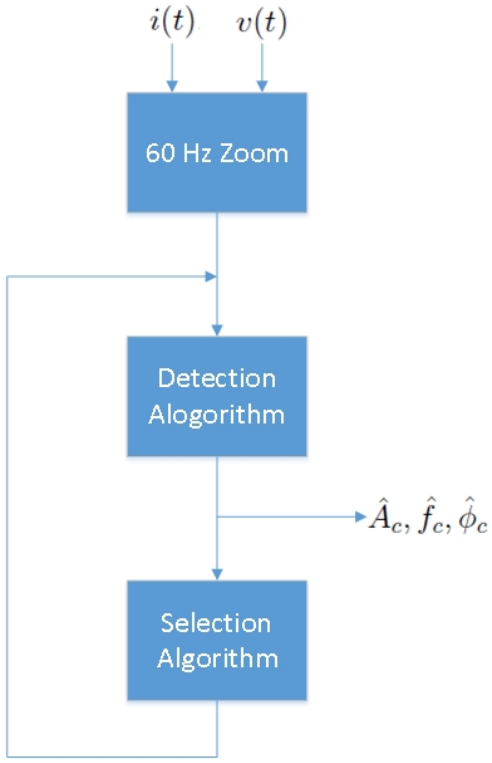

Figure 3.1: Block Diagram of Algorithm

The chapter is divided in three sections as the three blocks in figure 3.1. The first section explaining signal preprocessor to zoom in to 60 Hz frequency, the second details the detection algorithm and the next section illustrates the process of selection of rotor frequency and phase from others frequencies in the signal.

3.1 Preprocessor

The preprocessor comprises of a script developed by Professor Steven R. Shaw of the Montana State University [29] which takes in the measured stator current and voltage of the signal from PCI1710. This preprocessor was expressly used to compute current-harmonics of the common power source in this thesis. The preprocessor in fundamental terms, computes the Fourier coefficients of the signal (over a window) upto its 7th odd harmonic by integrating the product of the measured current waveform with a basis function line-locked to the measured voltage waveform over some finite interval (typically one or more periods of the fundamental frequency) [30]. It is essentially a homodyne detector(for amplitude demodulation of signal with frequency of interest i.e line frequency of 60 Hz) followed by low-pass filter(integrator).

The basis functions are typically sinusoids (having frequency equal to frequency of interest or carrier frequency) as motors consists of both resistive and reactive loads, the subsequent current drawn will have both sine and cosine terms. Cosine terms from resistive elements have zero degree phase and sine terms from reactive components have $\pm 90^{\circ}$ phases where pure inductive component changes the phase by -90 and a pure capacitive component changes it by +90. This when related to steady state power drawn can be represented by in-phase and quadrature elements. Hence, the current drawn in an induction motor can be represented from Eq.2.2.1 as:

$$x(t) = A_1 cos(\phi_0) cos(\omega_0 t) - A_0 sin(\phi_0) sin(\omega t) + A_1 cos(\phi_1) cos(\omega_1 t) - A_1 sin(\phi_1) sin(\omega_1 t) + ... \tag{3.1.1}$$

Modified (by multiplication of voltage for power), the Fourier coefficients also represent in-phase and quadrature components and real and reactive power for its cosine an and sine bn co-efficients respectively. The in-phase or real or resistive elements of

the current signal is computed using the following formula:-

$$a_n = \frac{P_n}{V} = \frac{1}{T}\int_T x(t) * cos(n\omega t)dt$$

Whereas the quadrature or reactive elements are computed as:-

$$b_n = \frac{Q_n}{V} = \frac{1}{T}\int_T x(t) * sin(n\omega t)dt$$

When substituting for the first harmonic (n=1) in equation 3.1.1 the above equations simplifies to [31]:-

$$P_1 = \frac{V}{T}\int_T A_0 cos(\phi_0) cos^2(\omega t)dt = \frac{VA_0 cos(\phi_1)}{2}$$

and

$$Q_1 = \frac{V}{T}\int_T A_1 sin(\phi_1) sin^2(\omega t)dt = \frac{-VA_0 sin(\phi_0)}{2}$$

Similarly, the preprocessor can compute other odd harmonics of the signal. As shown above the output from both phase locked in-phase and quadrature components results in accurate measurement of magnitude and phase of the carrier signal sans noise. The preprocessor computes the coefficients a_n and b_n over a moving window. This window, which is synchronized to the measured line voltage, is advanced every half-cycle. Thus,new coefficients are produced at twice the line frequency. For a 60Hz cycle, this implies that power estimates are produced at 120Hz [31].

3.2 Detection algorithm

The core of this thesis comprises of accurately detecting the frequency, phase and magnitude of the signal which emulates the speed of the individual induction motor. As the motors used in this thesis are 3-phase 4-pole induction motors, the frequency spectrum taken of their indivisual stator current correctly shows an amplitude spike

at around a maximum of 30Hz, i.e 1800 rpm. This maximum speed is calculated using the formula:

$$f = \frac{120 * Line\,frequency\,(F)}{Number\,of\,poles\,(P)}$$

The line frequency being 60Hz and number of poles being 4, this theoretical value comes out to be 30Hz which is the synchronous speed of the motor. When constrained with slip this speed drops depending on load and is referred as rotor frequency of the motor. The rotor eccentricity frequency is then half this value at 15Hz from Eq 1.3.2. However as the sampling frequency for all the experiments performed in this thesis is 120 Hz, the rotor eccentricity frequency now exists at 30 Hz.

When an aggregate measurement in taken, it comprises of signals of both the motors. Hence, first the frequency of one of the rotor eccentricity signal is determined using synchronous detection principle explained in section 2.3.2. To find this frequency, a range of frequencies (f_c) from 29 to 30 Hz (rotor frequency estimate) were converted to time domain signals ($cos(2\pi f_c t)$) with signal length being 1 minute and multiplied with the original signal. A 'for loop' is used in the Matlab code which loops through frequencies from 29 to 30 Hz in increments of 0.001 (i.e the resolution), as it was experimentally found the highest rotor eccentricity frequency which was the rotor eccentricity frequency under no-load condition was 29.99 Hz and the lowest (due to a load of 1 HP) was 29.4 Hz.

The low pass filter was modeled by a simple 'mean' operation in Matlab, which can be thought of as an integrator. The filter effectively blocks the high frequencies resulting from the mixer or multiplication as explained in section 2.3.2. As different values of f_c were looped through in $cos(2\pi f_c t)$, the dot product of this term and the signal resulted in one value at each loop. This value was the amplitude which maximized (largest of all values) when f_c equaled frequency of rotor eccentricity. Section 3.3 describes how the f_c which gives the maximum of these values is the rotor eccentricity frequency.

3.3 Selection Algorithm

Now, the result of the loop gave a range of values from among which the value that corresponds to rotor eccentricity frequency has to be selected. This objective is attained by using maximum-likelihood estimation principle [32]. This principle is used in signal detection theory where extracting a small signal embedded in noise is required. Although here the small signal is considered as rotor eccentricity signal whose frequency needs to be estimated. In conventional signal-detection theory the two signals, the noise and the low strength signal are identified as two hypotheses, H_1 and H_2. The main aggregate signal $i(t)$ ($x(t)$ in previous sections) can be written as:

$$i(t) = i_i(t) + i_c(t) + n(t)$$

where $i_i(t)$ is a signal consisting of all of the other components excluding $i_c(t)$ (the signal of interest) and $n(t)$, the random noise. In this context however we identify $i_c(t)$ as signal having rotor frequency f_c of motor 1(say). The mathematical hypotheses, H_1 and H_2 are:

$$H_1 : i(t) = i_i(t) + n(t)$$

$$H_2 : i(t) = i_i(t) + i_c(t) + n(t)$$

Here, H_1 is the null condition and thus assumes that $i_c(t)$ has not been transmitted and hypothesis H_2 assumes that it has.

In detection theory, a decision rule for a particular hypothesis, using the probability densities $p_1(i)$ and $p_2(i)$ of H_1 and H_2 over the interval (0:Tm), is developed to find which of hypothesis to be true. The probability densities are defined as:

$$p_1(i) = Fexp[-(1/N_0) \int_0^{T_m} (r(t) - i_i(t))^2 dt]$$

and

$$p_2(i) = Fexp[-(1/N_0)\int_0^{T_m}(r(t) - (i_i(t) + i_c(t)))^2 dt]$$

This decision is made by using maximum-likelihood estimation where the generalized likelihood ratio (GLR) is computed as:

$$\lambda_i = \frac{max_{param2}[p_2(i|param_2)]}{max_{param1}[p_1(i|param1)]}$$

We then find the value of param1, i.e parameter 1, that maximizes probability density p_1, and similarly we find the parameters (param2) which maximize probability p_2. The probability density definitions can be substituted in the above equation and the GLR can be written as:

$$\lambda_i = \frac{Fexp[-(1/N_0)\int_0^{T_m}(r(t) - (i_i(t) + i_c(t)))^2 dt]}{Fexp[-(1/N_0)\int_0^{T_m}(r(t) - i_i(t))^2 dt]}$$

Simplifying the above equation gives:

$$\lambda_i = exp[-(1/N_0)\int_0^{T_m}[-2r(t)i_c(t) + 2i_i(t)i_c(t) + 2i_c^2(t)dt]$$

Further, $i_i(t)i_c(t)$ is $i(t)$ which cancels over interval T_m and $i_c(t)$ can be written in the form:

$$i_c(t) = I_c sin(2\pi f_c t + \phi_c)$$

which when squared gives,

$$i_c^2(t) = I_c^2(T_m/2)$$

Substituting the above terms in equation and simplifying gives:

$$\lambda_i = exp(\frac{-I_c^2 T_m}{2N_0}) * exp(\frac{I_c}{N_0} \int_0^{T_m} 2r(t)sin(2\pi f_c t + \phi_c)dt)$$

Estimates for I_c (mag), f_c, and ph_c are obtained by maximizing the above equation. For a given I_c the equation maximizes when the integral term maximizes. We thus analyze this term separately [32]:-

$$\int_0^{T_m} 2r(t)sin(2\pi f_c t + \phi_c)dt = s(f_c)$$

$s(f_c)$ can be rewritten as:

$$s^2(f_c) = p^2(f_c) + q^2(f_c) = [\int_0^{T_m} 2r(t)sin(2\pi f_c t)dt]^2 + [\int_0^{T_m} 2r(t)sin(2\pi f_c t)dt]^2$$

where,

$$p(f_c) = s(f_c)cos\phi_c = \int_0^{T_m} 2r(t)sin(2\pi f_c t)dt$$

and

$$q(f_c) = s(f_c)sin\phi_c = \int_0^{T_m} 2r(t)cos(2\pi f_c t)dt$$

Hence when the above equation of $s^2(f_c)$ is used for (f_c) ranging from 29 to 30 Hz, the maximum of all the values of (f_c) is the highest frequency component in the range of 29 to 30, i.e the rotor eccentricity frequency.

Next, the phase of the rotor signal is calculated using similar equation for finding f_c but where the equation maximizes further when phase is matched:

$$s(f_c) = \int_0^{T_m} 2r(t)sin(2\pi f_c t + \phi_c)dt$$

In the above equation the previously computed value of fc is used. ϕ_c is looped from -180 to +180 degrees and the phase which maximizes $s(f_c)$ is the phase of the rotor eccentricity signal.

The amplitude of the signal is computed as:

$$mag = \frac{2\sqrt{(p|f_c, \phi_c)^2 + (q|f_c, \phi_c)^2}}{Length\, of\, signal}$$

Using the above estimates of frequency, phase and magnitude a signal with rotor eccentricity frequency and its corresponding time domain phase and magnitude can be generated. This time domain signal is then subtracted from the main signal which is then transformed to frequency domain to recover the rotor eccentricity frequency of the second motor. The precise estimation of signal parameters is key. It is unlikely that any two motors having the same load will have the exact rotor eccentricity frequency upto three decimals.

After subtraction of Motor 1 rotor eccentricity signal, the signal is then looped through frequency estimation part of the code again, which then estimates the rotor eccentricity frequency of Motor 2. The following chapter showcases matlab results of the two motors given different loads.

CHAPTER 4: EXPERIMENTAL RESULTS

This chapter illustrates how the experiment was setup, how the data was procured as well as the results of the experiment. It is divided into three sections. The first elaborates the experiment setup and equipment. The second, results of the experiment without any motor defects and third with a defected motor.

4.1 Experimental Setup

The experiment involves having two motors fed 3-phase power in parallel. The switch box consists of switches which splits the feed. Current transducers present on these channels (before and after the line was split) measure the current drawn by the motors. The sensor interface box then collects this data and enables connection to the computer via a SCSI cable. Figure 4.1 illustrates this process:-

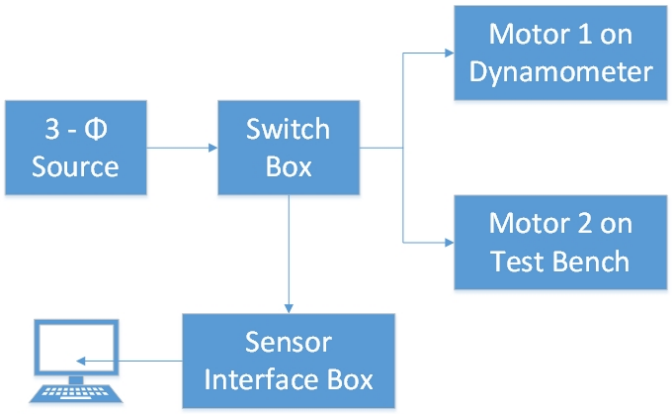

Figure 4.1: Block Diagram of experiment setup

The sensor interface box collects voltage and current measurements of the motors using voltage and current transformers respectively. The voltage transformer measures the input supply to the motor from two phases of the 3-phase supply. The first of the 3 current transformers, is placed on the supply line before it's split to be fed

in parallel to the motors, the second and third placed on each individual split lines fed to the two motors. A circuit diagram of this connection is given in figure 4.2:-

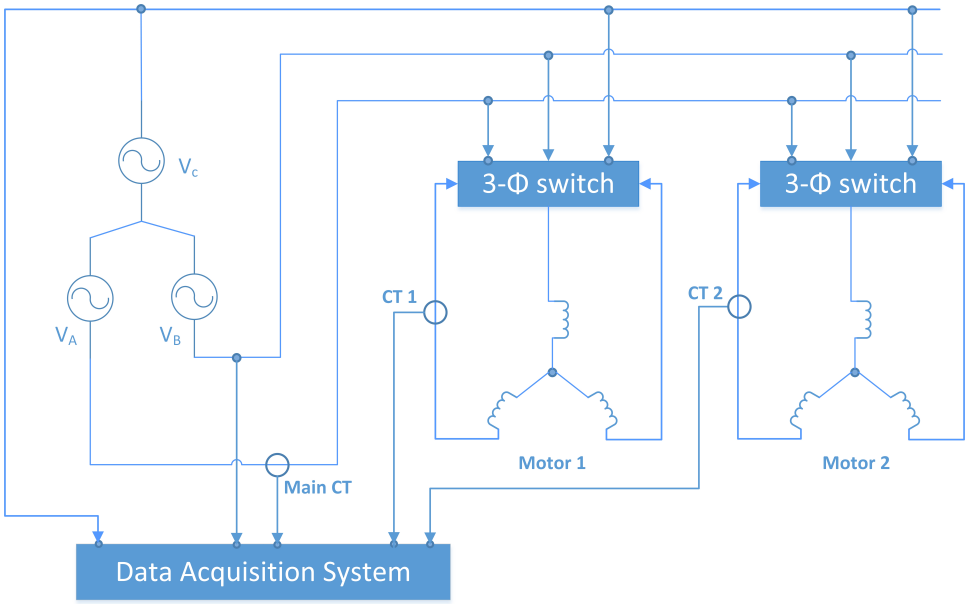

Figure 4.2: Circuit Diagram of experiment setup

The various equipment as well as boards used in this experiment are listed below:-

1. Power Supply: To obtain less noisy signal a three phase signal generator was used as input to the motors. This ensured the motor signal were not disturbed by stray grid frequencies or fluctuating grid voltages.

Figure 4.3: Power Supply to the Motors

2. The power from the generator was fed to the two motors in parallel. Figure 4.4

shows the three phase switches which split the incoming single line from the power supply into two.

Figure 4.4: Three phase switches splitting the line for parallel connection to the motors

3. Motor 1 supplied by switch 1 is set up to the dynamometer as shown in Figure 4.5.

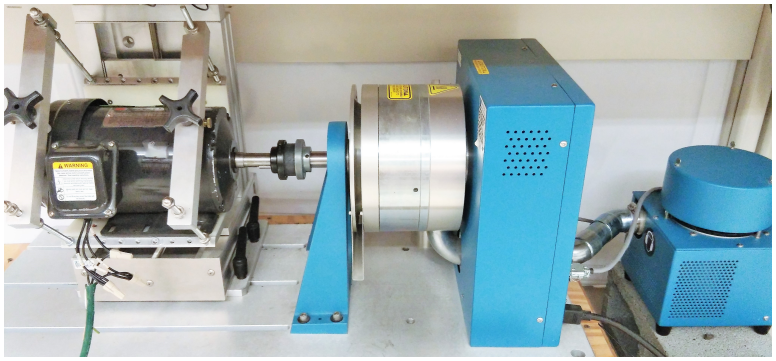

Figure 4.5: Motor 1 coupled to dyanamometer

4. The dynamometer is controlled by a controller wherein the load is regulated as required.

Figure 4.6: Controller for the dyanamomter, amount of torque generated by the load is controlled.

5. Motor 2 is coupled to a static load. However this load can be unbalanced to mimic a faulty set-up.

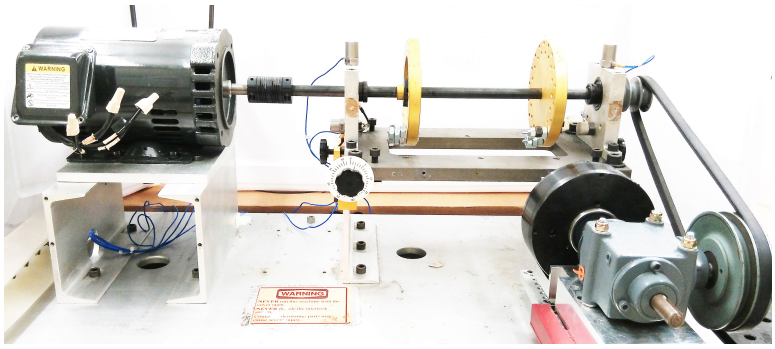

Figure 4.7: Motor 2 coupled to external load

6. Current and Voltage transducers were used to detect current and voltage respectively drawn by the motors and were the main data acquisition component. Figure 4.8 below illustrates the specifications of the transducers:-

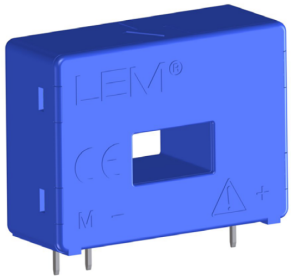

Electrical data

I_{PN}	Primary nominal rms current				50		A
I_{PM}	Primary current, measuring range				0 .. ±70		A
R_M	Measuring resistance @		T_A = 70 °C		T_A = 85 °C		
			$R_{M\,min}$	$R_{M\,max}$	$R_{M\,min}$	$R_{M\,max}$	
	with ±12 V	@ ±50 A_{max}	10	100	60	95	Ω
		@ ±70 A_{max}	10	50	60 [1]	60 [1]	Ω
	with ±15 V	@ ±50 A_{max}	50	160	135	155	Ω
		@ ±70 A_{max}	50	90	135 [2]	135 [2]	Ω
I_{SN}	Secondary nominal rms current				50		mA
K_N	Conversion ratio				1 : 1000		
U_C	Supply voltage (±5 %)				±12 .. 15		V
I_C	Current consumption				10 (@ ±15 V) + I_S		mA

(a) Current transducer used in this thesis

Electrical data

I_{PN}	Primary nominal r.m.s. current		10		mA
I_P	Primary current, measuring range		0 .. ± 14		mA
R_M	Measuring resistance		$R_{M\,min}$	$R_{M\,max}$	
	with ± 12 V	@ ± 10 mA_{max}	30	190	Ω
		@ ± 14 mA_{max}	30	100	Ω
	with ± 15 V	@ ± 10 mA_{max}	100	350	Ω
		@ ± 14 mA_{max}	100	190	Ω
I_{SN}	Secondary nominal r.m.s. current		25		mA
K_N	Conversion ratio		2500 : 1000		
V_C	Supply voltage (± 5 %)		± 12 .. 15		V
I_C	Current consumption		10 (@±15V) + I_S		mA
V_d	R.m.s. voltage for AC isolation test [1], 50 Hz, 1 mn		2.5		kV

(b) Voltage transducer used in this thesis

Figure 4.8: Current and Voltage transducers used in the experiment and their specifications

7. A SCSI cable was used to transfer the stator current signals from the motors to the computer. An AC to DC converter gives DC power supply to the board for the voltage transducers. The circuit board is pictured in Figure 4.9:-

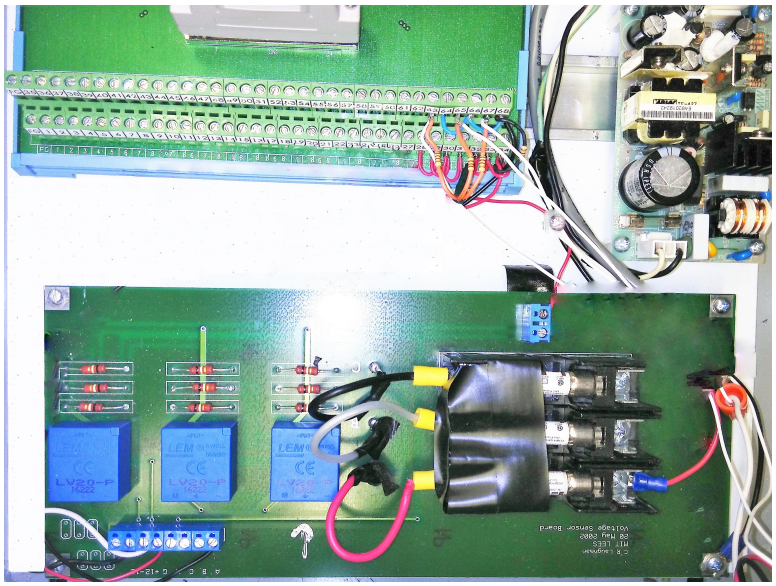

Figure 4.9: Main data acquisition board

8. The PCI-1710 card in the computer samples the analog signal at 50000 hz divided across all channels (Number of channels being 6: 3 current and 3 voltage channels for 3 current transducers and 3 voltage transducers respectively). The frequency as well as the number of channels to be considered is set by NILM (non-intrusive load monitor) software.

9. The data is further processed by the preprocessor software in NILM.

4.2 Initial Motor Results

To test the effectiveness of the algorithm, both motors were operated simultaneously under varying load conditions. Motor 2, which is located on the test bench, operates with an approximately constant 120W load and thus its speed was approximately constant. Since motor speed is related to load, we changed the speed of Motor 1 by adjusting the load on the dynamometer attached to it. Initially, Motor 1 was loaded at 50W and the load was gradually increased in 5W steps until the load on the two motors became approximately equal at 120W. The load was then more rapidly increased until 600W. Since the two motors are the same model, we thus expect the speed of Motor 1 to initially be higher than that of Motor 2 and eventually become slightly lower as the load passes above 120W.

Tests were performed to compare the results of the proposed algorithm to those of a more standard DFT-based approach. We thus analyzed the data using two different methods:

1. Method 1: Initial 60Hz zoom followed by the DFT

2. Method 2: Proposed tracking algorithm (Chapter 3)

Analysis was performed using both methods at each of the load levels identified in Table 4.1. The DFT of the individual CT signal was used to verify the speed of the two machines. Data was initially recorded for both one minute and two minute intervals at each load level.

Table 4.1: Table of power values given to dyanamometer on Motor 1 and the torque generated by Motor 1 to overcome this load.

Test No.	Electrical Load Generated (W)	Motor Torque (Nm)
1	50W	0.268 Nm
2	55W	0.295 Nm
3	60W	0.320 Nm
4	65W	0.350 Nm
5	70W	0.375 Nm
6	75W	0.400 Nm
7	80W	0.427 Nm
8	85W	0.452 Nm
9	90W	0.480 Nm
10	95W	0.508 Nm
11	100W	0.533 Nm
12	120W	0.640 Nm
13	150W	0.800 Nm
14	170W	0.906 Nm
15	200W	1.068 Nm
16	300W	1.603 Nm
17	600W	3.230 Nm

With both Method 1 and Method 2, an initial zoom was performed using the preprocessor algorithm described in Chapter 3. The effect of this can be seen by examining the aggregate current given previously in Equation 2.1.2. For simplicity, we neglect the additional term $i_X(t)$ (where $i_X(t)$ is all other signals in the current

waveform) and write this as:-

$$i_S(t) = I_1 \cos(\omega_e t + \phi_1) + I_{h,1A} \cos((\omega_e + \omega_{r,1A})t) + I_{h,1B} \cos((\omega_e + \omega_{r,1B})t)$$

After applying the zoom, the initial coefficient $a_1(t)$ will have the form

$$a_1(t) = I_1 \cos(\phi_1) + I_{h,1A} \cos(\omega_{r,1A}) + I_{h,1B} \cos(\omega_{r,1B}) \tag{4.2.1}$$

This allows the initial 8kHz data to be downsampled to 120Hz, which simplifies off-line data analysis. Note that the use of the preprocessor demodulates the current signal and thus relocates the eccentricity-related signals to a lower frequency. For the 4-pole motor selected here, this means that the two speed signals should be located slightly below 30Hz in $a_1(t)$. As an example, consider the results shown in Figure 4.10. These two graphs show the DFT of the preprocessed signal $a(t)$ for the two individual CTs. Note that the eccentricity-related signals are located just below 30Hz as expected. Measurement with a tachometer verified that these frequencies matched the actual motor speeds. Throughout the remainder of this section, we report the actual motor speed using the DFT of the individual CT signals. A table associating motors to their corresponding Current transformer is given as follows:-

Table 4.2: Motor number and their corresponding CT

Source	Current Transformer
Aggregate Current	CTm
Motor 1 Current	CT1
Motor 2 Current	CT2

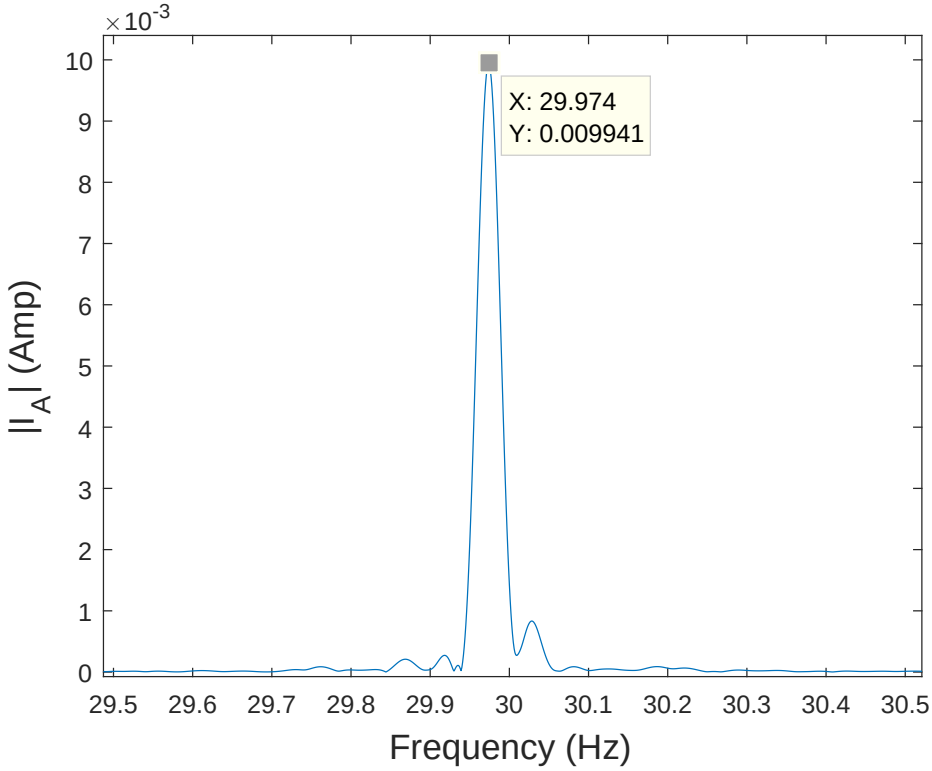

(a) DFT of data from CT1 showing rotor eccentricity frequency of motor 1 with 50W load.

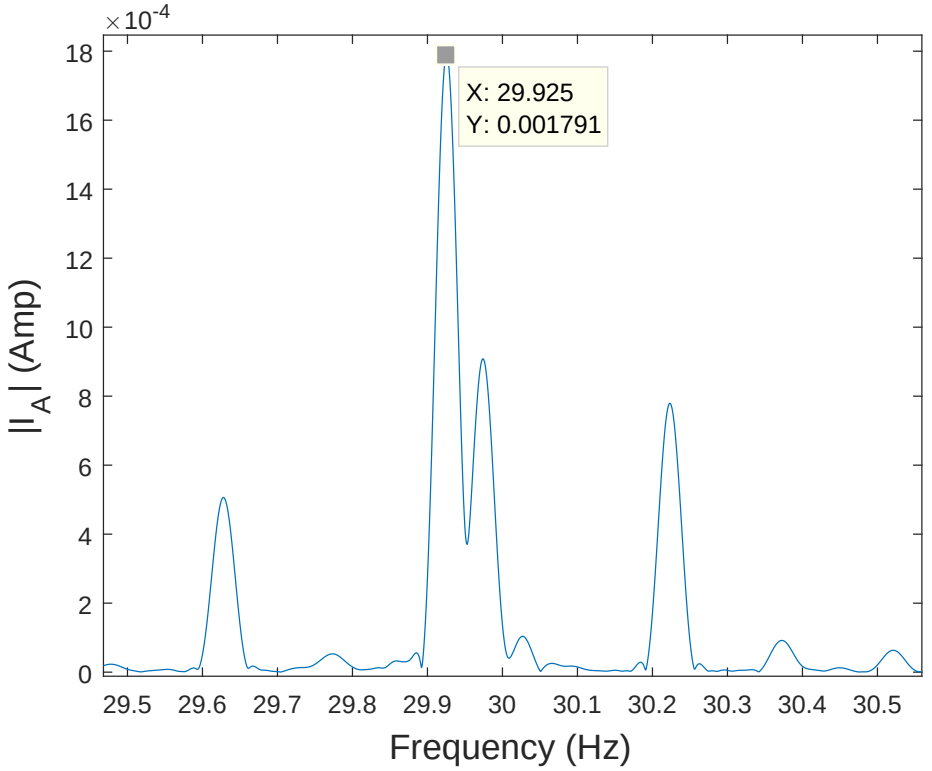

(b) DFT of data from CT2 showing rotor eccentricity frequency of motor 2 with a constant load of 120W

Figure 4.10: DFT of individual CT signals showing frequency of rotor eccentricity

4.2.1 50W Load Condition Results

Table 4.2 shows the measured speed of the two motors during the 50W test as shown in Figure 4.10 above. As expected, Motor 1 runs with a slightly higher speed than Motor 2 due to smaller load. Figure 4.11 shows the corresponding DFT obtained using Method 1. Note that several distinct peaks are observed. As expected, two of these peaks are located at the measured motor speeds. In addition, however, there are also peaks at other frequencies above 30Hz. Note that we know to ignore these signals since it is not possible for a four-pole motor connected to a 60Hz supply to spin above 30Hz. In this case, the peak caused by Motor 2 (i.e. the one at 29.922Hz) is much smaller than the one caused by Motor 1. This is likely because it naturally has slightly more eccentricity than Motor 2. Such differences are to be expected between two different motors of the same make and model.

Table 4.3: Rotor eccentricity frequency of individual motors for 50W load

Rotor Frequency for 50W load	Frequency(Hz)
Motor 1	29.974
Motor 2	29.926

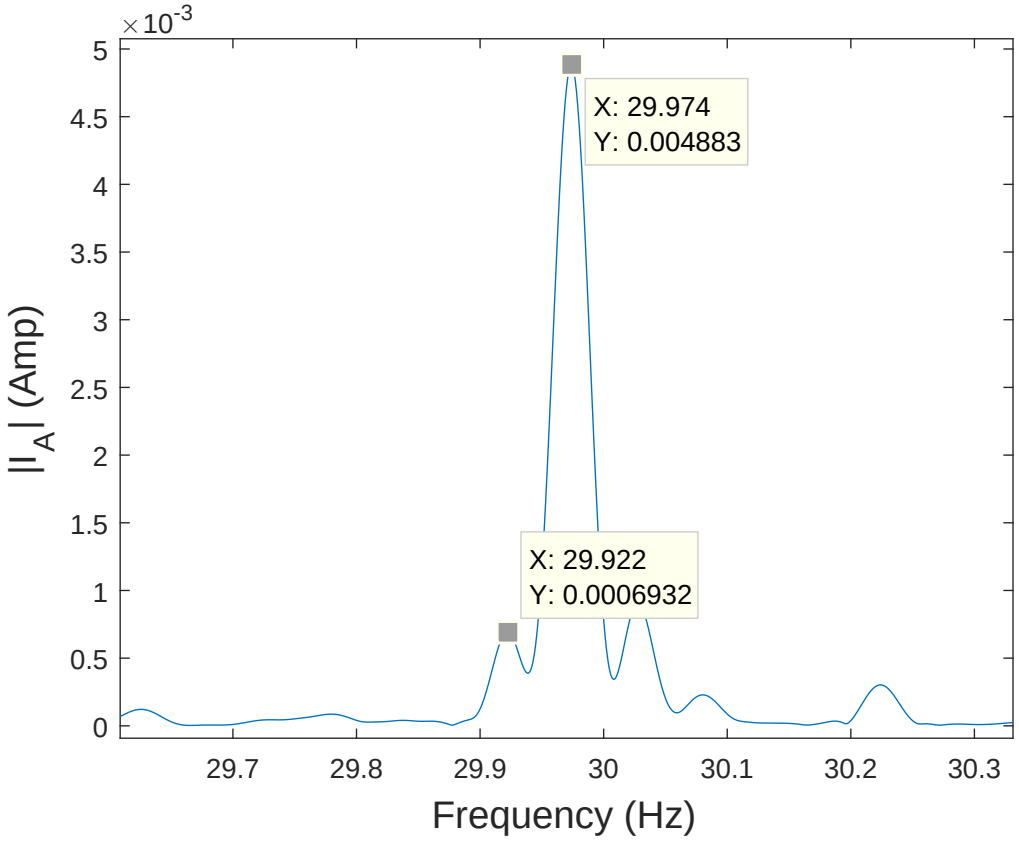

Figure 4.11: FFT of Current from main CTm

When using Method 2, we first apply the FFT zoom and the use the detection algorithm to obtain one of the motor peaks. Recall that we then subtract this signal from $a_1(t)$ and then attempt to apply the detection algorithm a second time to obtain the other motor peak. Figure 4.12 shows the results after the first signal has been subtracted from the aggregate. If we thus compare Figure 4.11 to Figure 4.12, we see that large peak from Motor 1 at 29.974 Hz has been drastically reduced because of the subtraction. Now, we can clearly see the signal at 29.925Hz, which is taken as the eccentricity-related signal generated by Motor 2. Figure 4.13 shows the resulting MATLAB output from the tracking algorithm code. Note that the two frequencies of interest have been obtained.

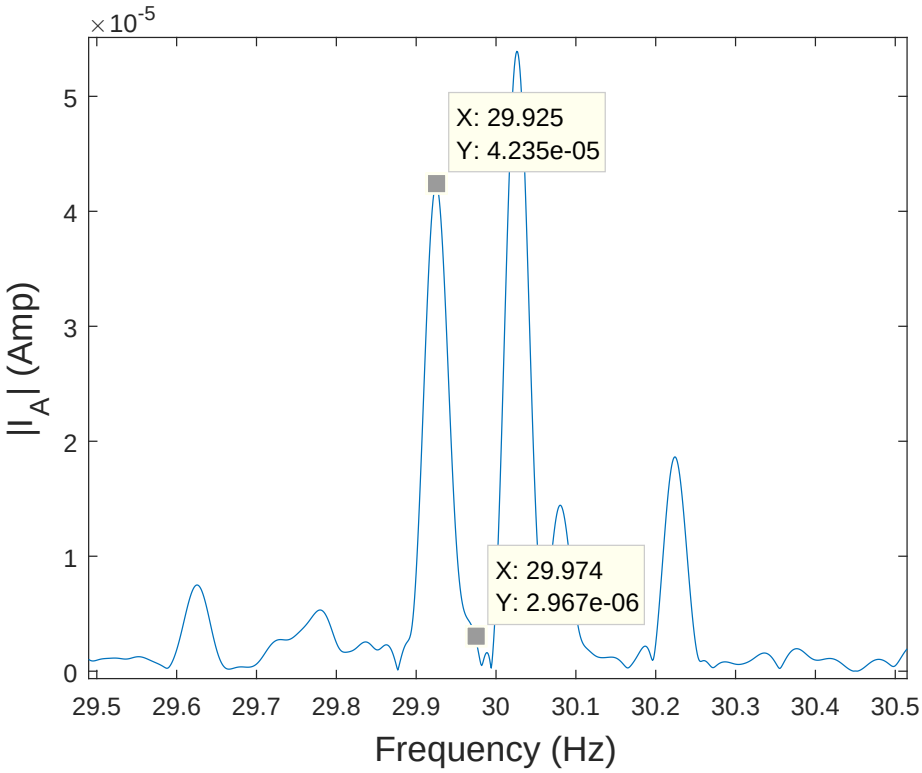

Figure 4.12: FFT of data from CT1 after rotor frequency of motor 1 has been subtracted.

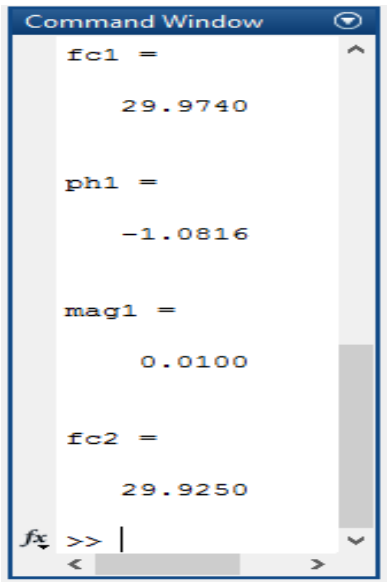

Figure 4.13: Results of Zoom FFT algorithm where f_{c1} is rotor frequency of motor 1 and f_{c2} of motor 2, ph_1 and mag_1 is phase and magnitude of motor 1 used to form time domain signal to subtract from CT1 data.

4.2.2 70W Load Condition Results

Table 4.2 shows the measured speed of the two motors during the 70W test. As expected, the two motor speeds have moved closer. Figure XXX shows the corresponding DFT obtained using Method 1 with one-minute of measured data. Note that the signal generated by Motor 1 has become so close to that of Motor 2 that we can no longer safely distinguish between the signals using the DFT. If we apply Method 1 to two minutes of measured data, however, we obtain the results shown Figure 4.14 (b). Note that with more data, the effects of windowing have been reduced and thus the two frequencies are more clearly distinguishable. In practice, the use of additional data is not always a feasible solution. As the load on Motor 1 increased above 70W toward 120W, it was no longer possible to use Method 1 to distinguish between the two motors when using 1 minute of data. The issue about data length is discussed further in later sections.

Table 4.4: Rotor eccentricity frequency of individual motors for 70W load

Rotor Frequency for 70W load	Frequency(Hz)
Motor 1	29.962
Motor 2	29.929

Although Method 1 could not uniquely distinguish the two peaks when Motor 1 was operating at 70W, Method 2 was able to do so. The following figure shows rotor eccentricity frequencies of two motors merging into each other from DFT of main CT (CTm) signal.

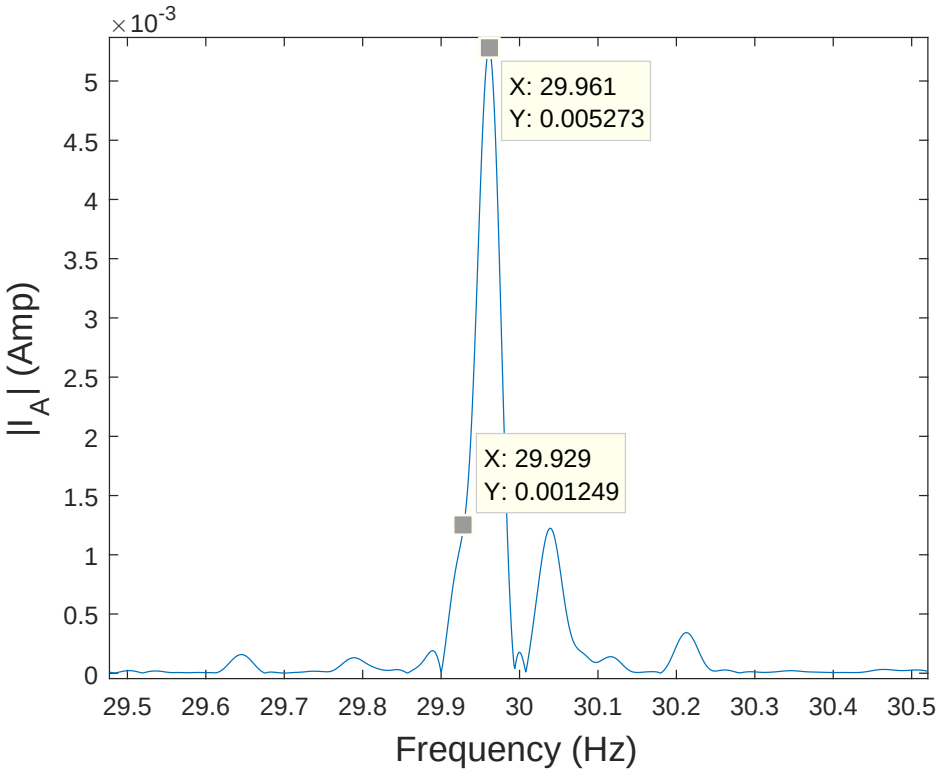

(a) DFT of main CT (CTm) signal for 70W load run for 1 minute

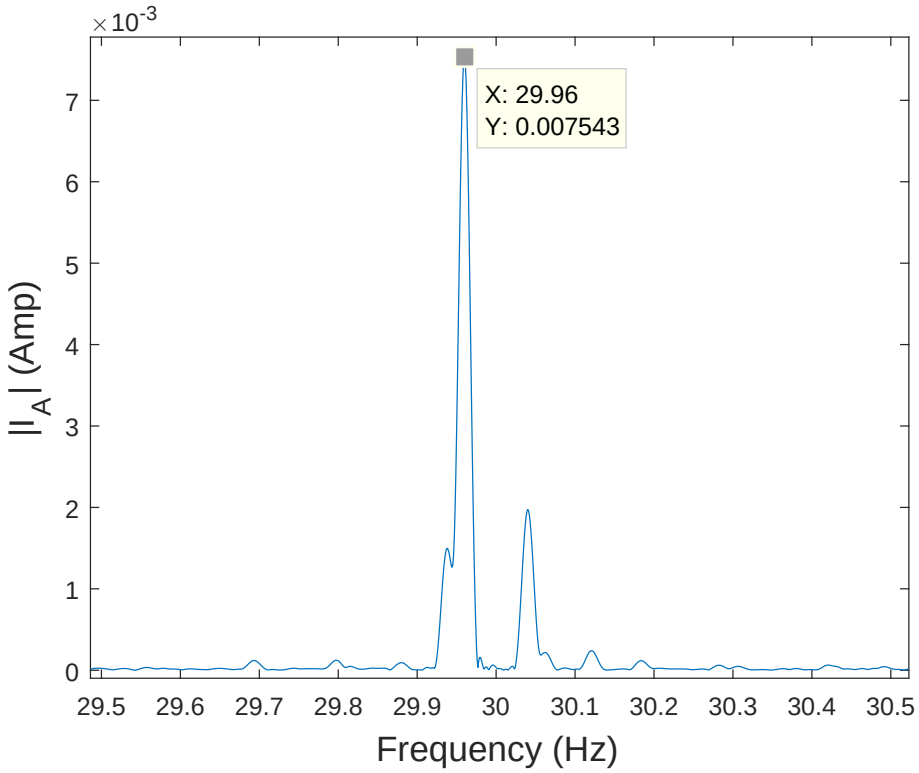

(b) DFT of main CT (CTm) signal for 70W load run for 2 minute

Figure 4.14: DFT of data from CTm at 70W showing more distinct Motor 2 eccentricity frequency for 2 minute

Figure 4.15 shows the DFT of $a_1(t)$ once the signal from Motor 1 has been subtracted. Once again, note that the signal generated by Motor 1 has been significantly reduced and the signal for Motor 2 at 29.929Hz is clearly visible.

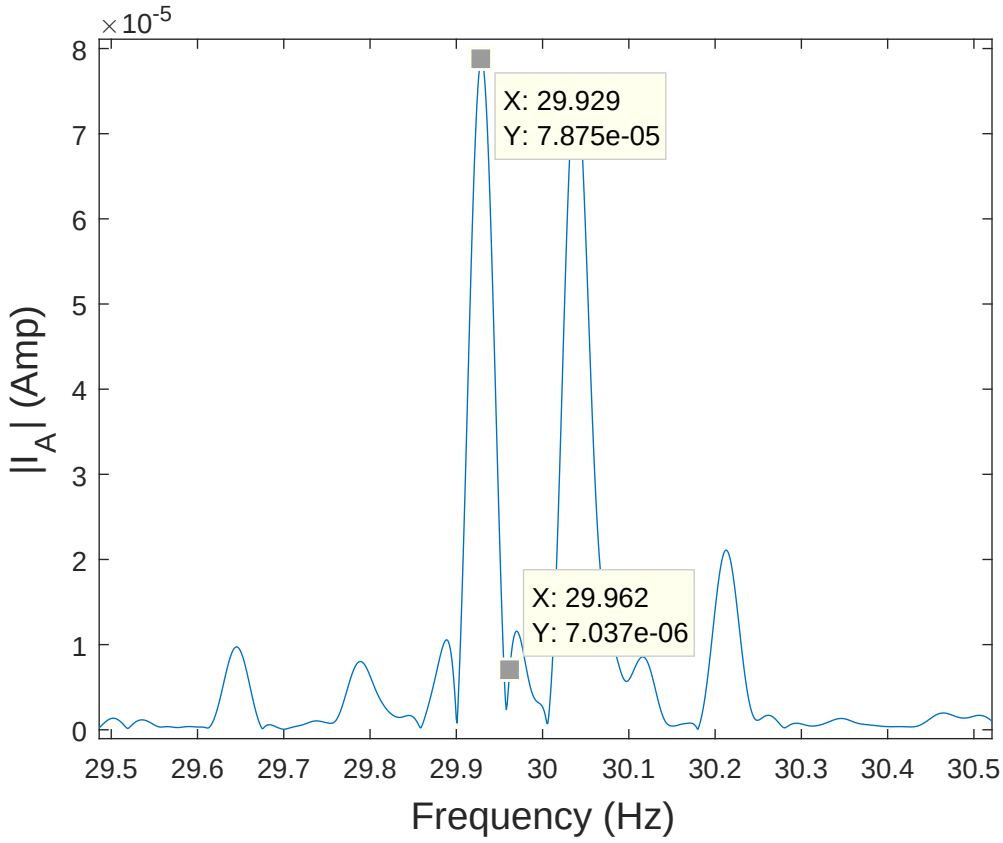

Figure 4.15: FFT of data from CT1 after rotor frequency of motor 1 has been subtracted.

Results of proposed tracking algorithm:-

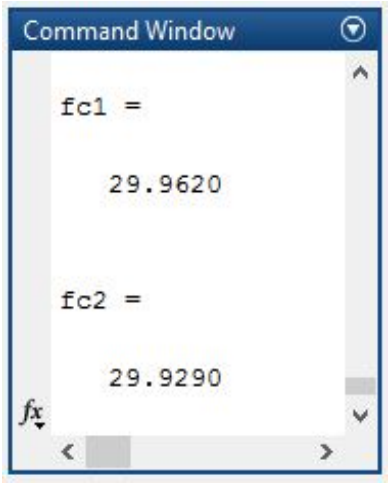

Figure 4.16: Results of Proposed tracking algorithm where f_{c1} is rotor frequency of motor 1 and f_{c2} of motor 2

4.2.3 120W Load Condition Results

Table 4.4 shows the measured speed of the two motors for a load of 120W. Note that the constant load on Motor 2 is 120W as well. This particular load condition is therefore selected to be displayed as both loads are almost equal, with motors speeds within 0.002 Hz frequency difference. As can be seen in Figure 4.17, the two frequencies marked overlap as well, concealing the plot below. Hence the figure is zoomed in further in 4.17 (b).

Table 4.5: Rotor eccentricity frequency of individual motors for 120W load

Rotor Eccentricity Frequency for 120W load 1 min data	Frequency(Hz)
Motor 1	29.929
Motor 2	29.931

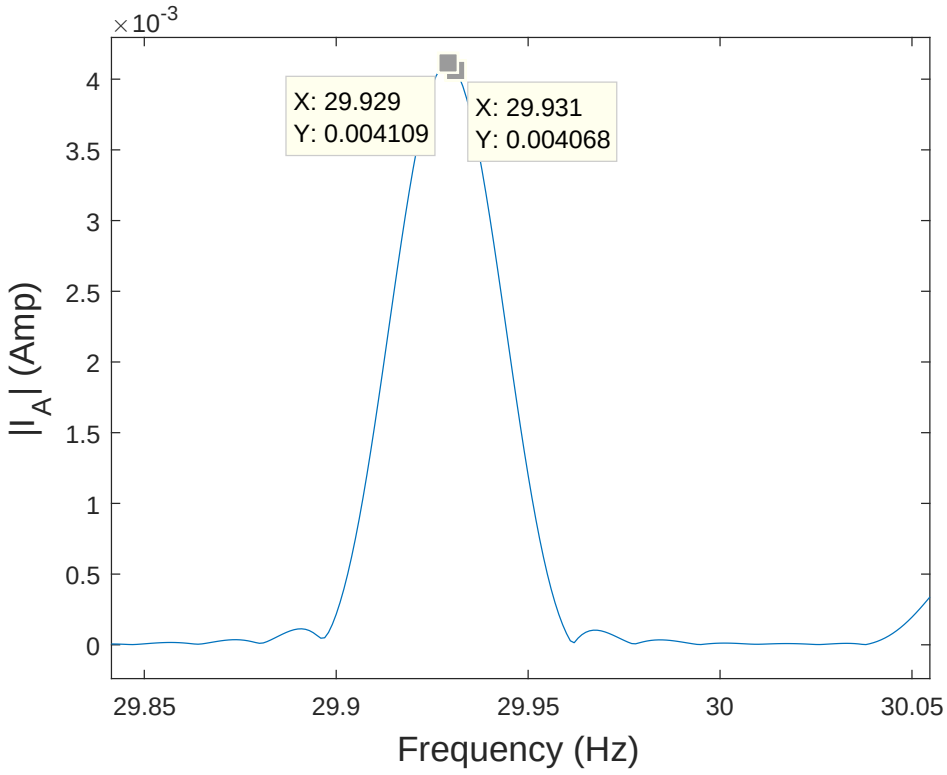

(a) DFT of data from CTm for 120W load run for 1 minute

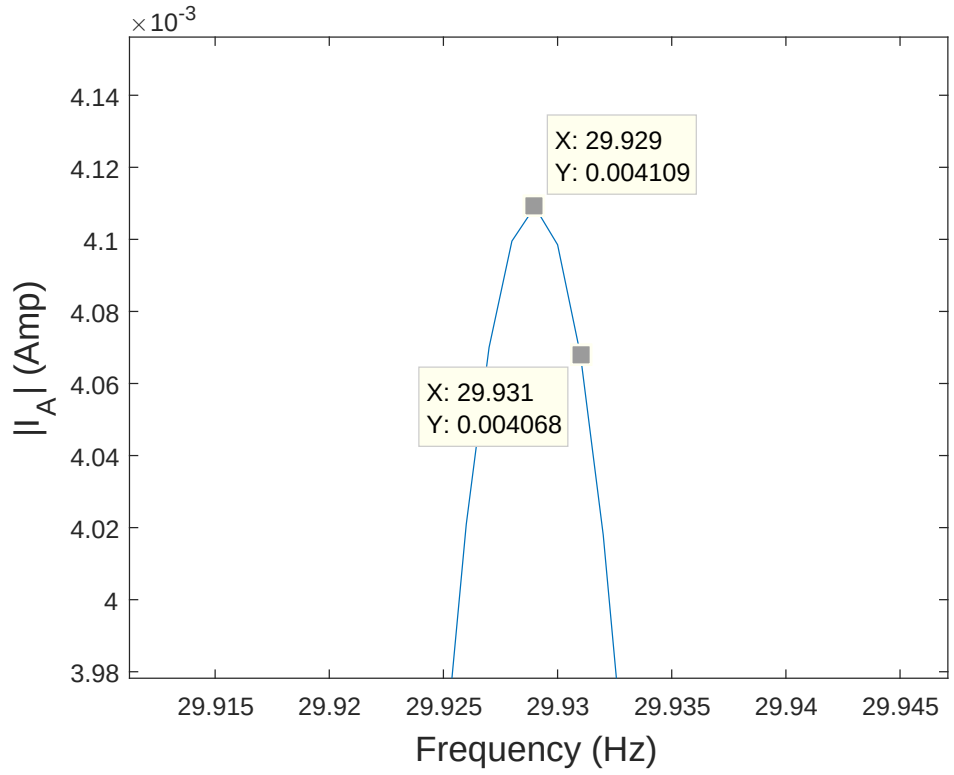

(b) Zoomed-in image of the above figure

Figure 4.17: DFT of data from CTm at 120W marking where rotor-eccentricity frequencies should be for Motor 2

The proposed tracking algorithm is also unable to detect the correct rotor eccentricity frequency using 1 minute of data because subtracting Motor 1 signal results in Motor 2 signal also getting subtracted. This can be thought of as not having enough data in the main signal for separate motor frequencies and they instead combine to form one. Figure 4.18 shows the subtracted signal and Figure 4.19 the output of tracking algorithm.

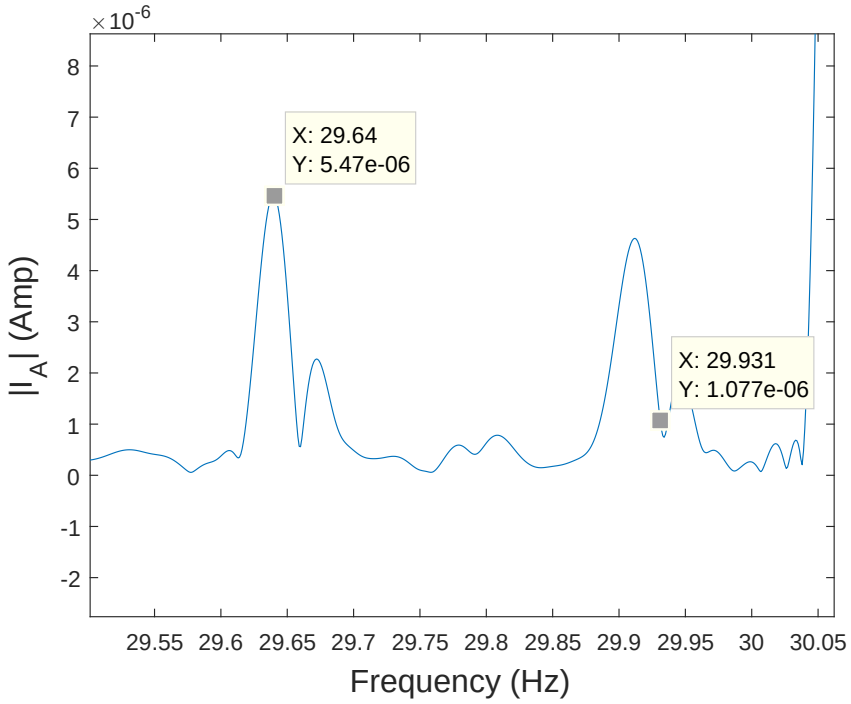

Figure 4.18: DFT of subtracted signal for 120W load of 1 minute data length

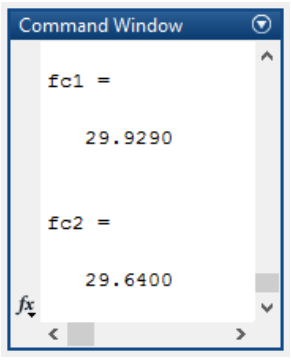

Figure 4.19: Results of tracking algorithm for 120W load where f_{c1} is rotor frequency of motor 1 and f_{c2} of motor 2. Here, f_{c2} should be 29.931

Increasing the data length to two minutes does not add any considerable distinguishing feature to the DFT obtained using Method 1 as shown in Figure 4.20, however Method 2 now gives the Motor 2 eccentricity frequency. Figure 4.21 shows the correctly subtracted signal displaying peak at 29.936, quite close to actual frequency of 29.935 for 2 minute data.

Table 4.6: Rotor eccentricity frequency of individual motors for 120W load run for 2 minutes

Rotor Eccentricity Frequency for 120W load 2 min data	Frequency(Hz)
Motor 1	29.927
Motor 2	29.935

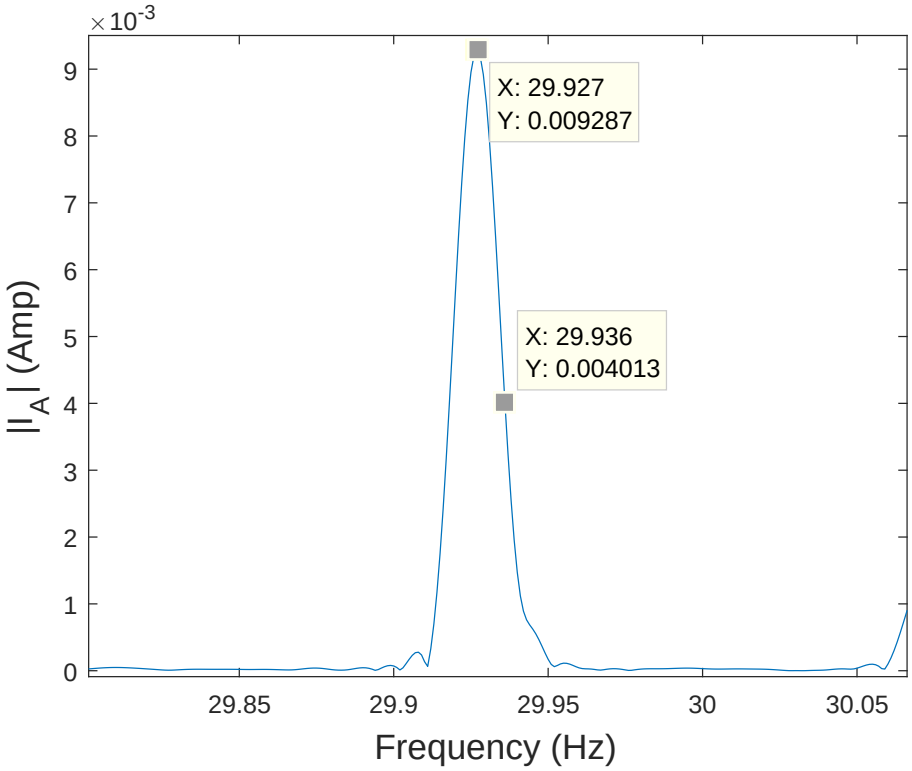

Figure 4.20: DFT of CTm at 120W load for 2 minute

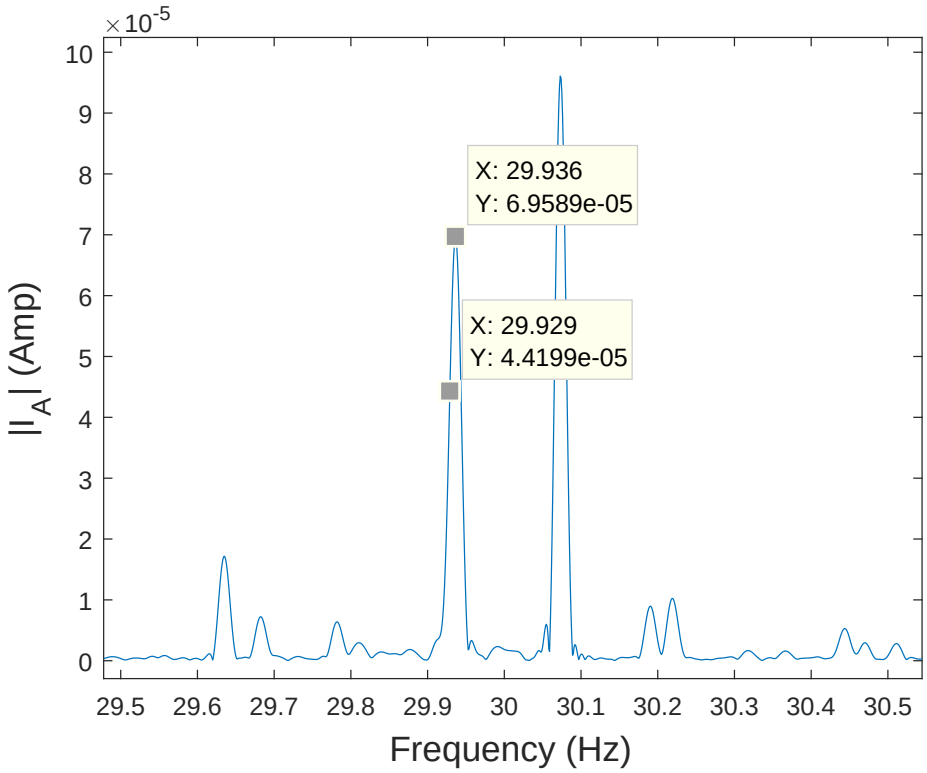

Figure 4.21: DFT of signal after Motor 1 rotor eccentricity signal has been subtracted

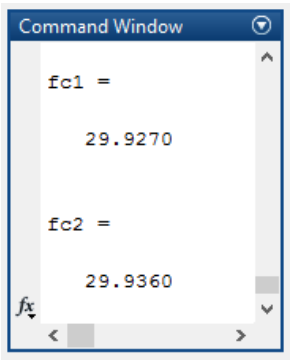

Figure 4.22: Output of tracking algorithm where f_{c1} is rotor eccentricity frequency of Motor 1 and f_{c2} of Motor 2

The following tables list Rotor speeds for all load conditions. Table 4.6 lists the speed results for both motors run for 1 minute with a load condition. Here, second columns shows the load value, third displays the measured speed of the Motor 1 by individual CT, fourth column of "FFT Est. Speed" gives DFT of main CT (CTm) and displays the result of motor speed from its graph, the next column "Code Est

Speed" gives the result of tracking algorithm. Motor 2 speeds are displayed in the next three columns.

Table 4.7: This table contains results of the experiment with 1 min data

Test	Load	Motor 1			Motor 2		
Number	(Watt)	Measured Speed (Hz)	FFT Est. Speed (Hz)	Code Est. Speed (Hz)	Measured Speed (Hz)	FFT Est. Speed (Hz)	Code Est. Speed (Hz)
1	50	29.974	29.974	29.974	29.925	29.925	29.925
2	55	29.971	29.971	29.971	29.927	29.930	29.928
3	60	29.968	29.968	29.968	29.968	29.929	29.929
4	65	29.965	29.965	29.965	29.928	n/a	29.928
5	70	29.961	29.961	29.962	29.929	n/a	29.929
6	75	29.959	29.958	29.959	29.937	n/a	29.931
7	80	29.955	29.956	29.955	29.938	29.92	29.932
8	85	29.952	29.951	29.952	29.930	n/a	29.932
9	90	29.948	29.946	29.948	29.932	n/a	29.931
10	95	29.942	29.943	29.943	29.936	n/a	29.928
11	100	29.942	29.942	29.942	29.945	n/a	29.927
12	120	29.929	29.929	29.929	29.931	n/a	n/a
13	150	29.909	29.908	29.908	29.933	n/a	29.928
14	170	29.895	29.895	29.895	29.935	n/a	29.927
15	200	29.874	29.873	29.873	29.931	29.931	29.931
16	300	29.804	29.804	29.804	29.803	29.931	29.931
17	600	29.578	29.578	29.578	29.938	29.938	29.938

Table 4.7 lists the motor speeds when run for 2 minutes with the same load.

Table 4.8: This table contains results of the experiment with 2 min data

Test	Load	Motor 1			Motor 2		
Number	(Watt)	Measured Speed (Hz)	FFT Est. Speed (Hz)	Code Est. Speed (Hz)	Measured Speed (Hz)	FFT Est. Speed (Hz)	Code Est. Speed (Hz)
1	50	29.973	29.973	29.973	29.938	29.937	29.938
2	55	29.970	29.970	29.970	29.938	29.939	29.938
3	60	29.967	29.967	29.967	29.939	29.939	29.938
4	65	29.963	29.963	29.963	29.939	29.938	29.939
5	70	29.960	29.960	29.960	29.939	29.938	29.939
6	75	29.956	29.956	29.957	29.939	n/a	29.945
7	80	29.953	29.953	29.953	29.938	29.934	29.940
8	90	29.947	29.945	29.946	29.940	n/a	29.938
9	95	29.941	29.943	29.943	29.940	n/a	29.936
10	100	29.940	29.940	29.940	29.938	n/a	29.934
11	120	29.927	29.926	29.927	29.935	n/a	29.936
12	150	29.906	29.906	29.906	29.939	29.937	29.939
13	170	29.892	29.892	28.892	29.939	29.939	29.939
14	200	29.871	29.871	29.871	29.939	29.939	29.939
15	300	29.801	29.801	29.801	29.939	29.939	29.939
16	600	29.578	29.578	29.578	29.939	29.939	29.939

4.3 Faulted Motor Results

This section documents the results when Motor 2 load is radially unbalanced to induce eccentricity. Recall that Motor 2 is placed on a test bench having constant

load. This load can be unbalanced by inserting weights on one side of the load. Figure 4.23 shows how this was achieved in the lab.

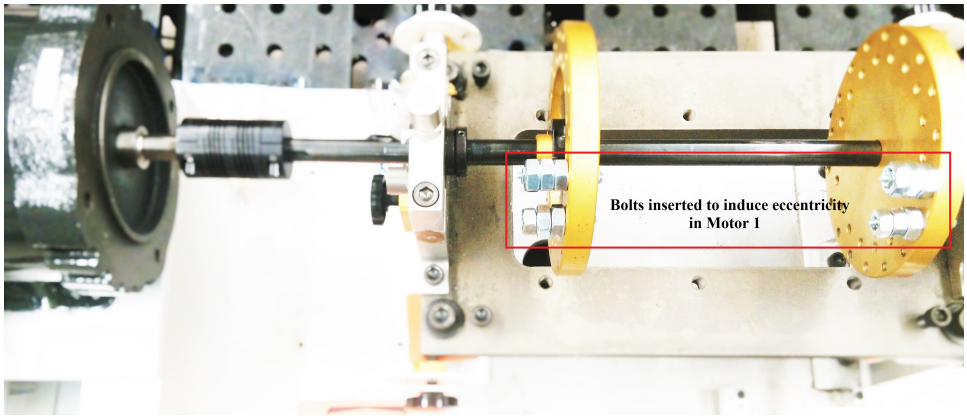

Figure 4.23: Induced fault in Motor 2

As discussed in section 3.2 air-gap eccentricity frequencies always exist in any motor. Manufacturers tend to keep eccentricity as low as possible with maximum permissible limit of 10% of nominal radial airgap length [22]. To study the efficacy of the tracking algorithm at high air-gap eccentricity the same load conditions are re-run for Motor 1, however Motor 2 now has induced eccentricity.

These eccentricity signals of Motor 2 now have increased magnitude as its rotor vibrates with the eccentric load and hence draws more current. Taking a simple example, we test this theory by having same load condition for Motor 1 whereas Motor 2 first has a constant load and then eccentricity induced load. DFT of aggregate current is shown in Figure 4.24 (Motor 2 without induced eccentricity) and Figure 4.25 (Motor 2 with induced eccentricity).

In Figure 4.24, Motor 2 eccentricity frequency in the DFT of aggregate current has an amplitude of 0.0006 A whereas in Figure 4.25 this amplitude has increased to 0.02243 A. It should be noted that Motor 1's amplitude of rotor eccentricity did not significantly change.

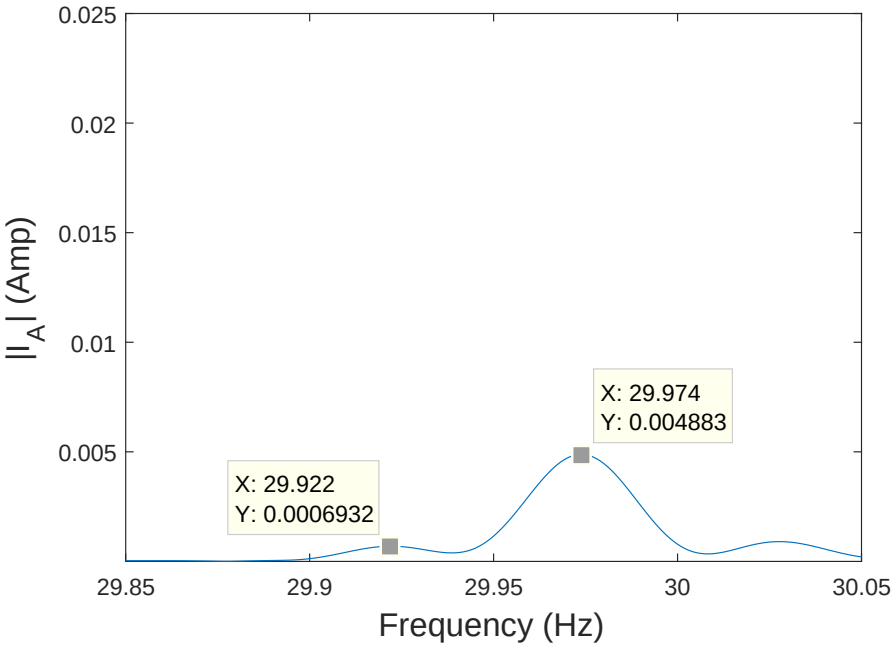

Figure 4.24: DFT of aggregate current for 50W load on Motor 1 and 120W constant load on Motor 2

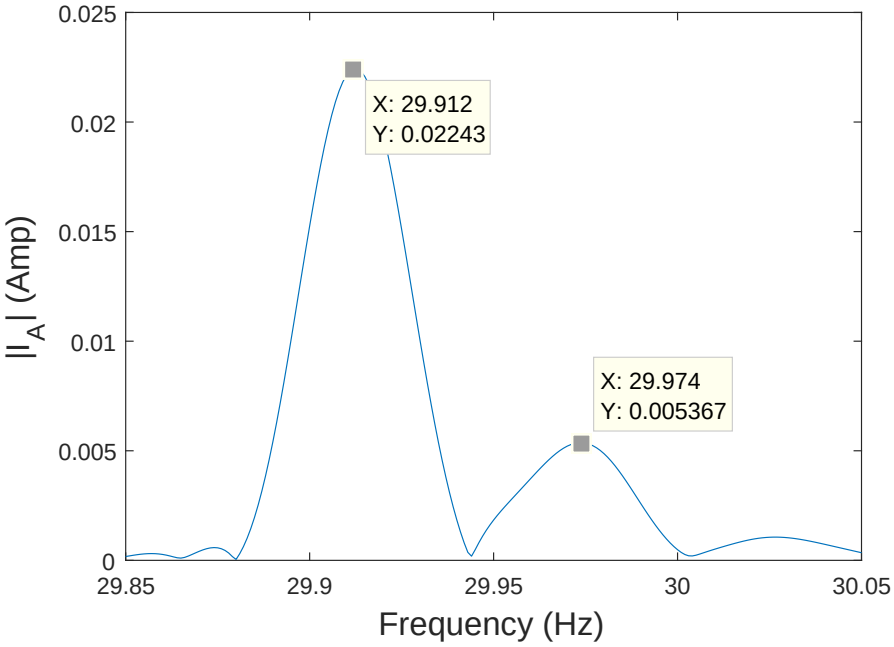

Figure 4.25: DFT of aggregate current for 50W load on Motor 1 and 120W faulted load on Motor 2

As can be seen from the above figures, frequency of the motors could be tracked

pretty efficiently by both Method 1 (where it detects Motor 2 frequencies, refer Table 4.7) and Method 2. However to effectively detect rotor eccentricity signal, its amplitude needs to be identified as well. Tracking amplitudes does not give consistent results as rotor eccentricity signal is seldom a sinusoid and varies with rotor oscillation. However amplitude tracked by Method 2, i.e the proposed algorithm is seen to be in close vicinity of individual motor rotor eccentricity signal amplitude.

Figure 4.26 shows result of detection of magnitude of Motor 2 eccentricity frequency (from aggregate current) with loads from 50 W to 170 W (10 W interval) run for 2 minutes in blue. The red plot in Figure 4.26 indicates DFT of the same loading and time conditions of Motor 2 from its individual CT (CT2). Note that here Motor 2 does not have an induced fault.

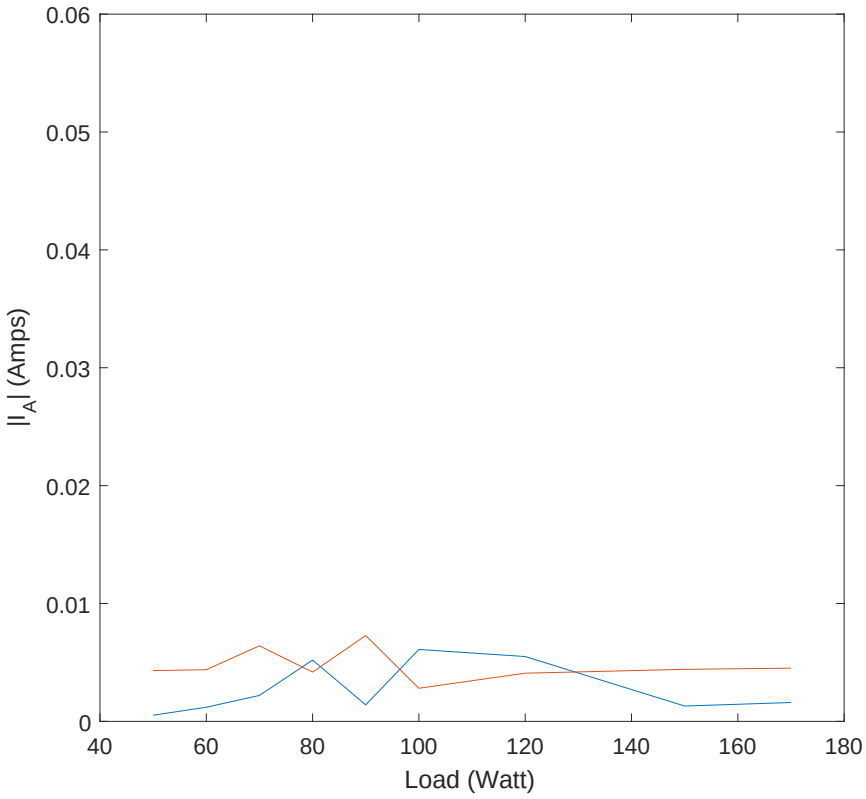

Figure 4.26: Blue: Amplitude detected by proposed algorithm using aggregate current. Red: DFT of Motor 2 eccentricity signal from individual CT1.

As can be seen from the above figure, both the methods have detected amplitude values to be between 0 and 0.01. Figure 4.27 plots amplitude values for Motor 2 with induced fault. Here as well blue plot reflects results of the tracking algorithm and red results of DFT of Motor 2 (data length is 1 minute). Expectedly, the amplitudes are now higher and range between 0.02 to 0.05. Proposed algorithm tracks the DFT significantly better than Motor 2 when it had no induced faults.

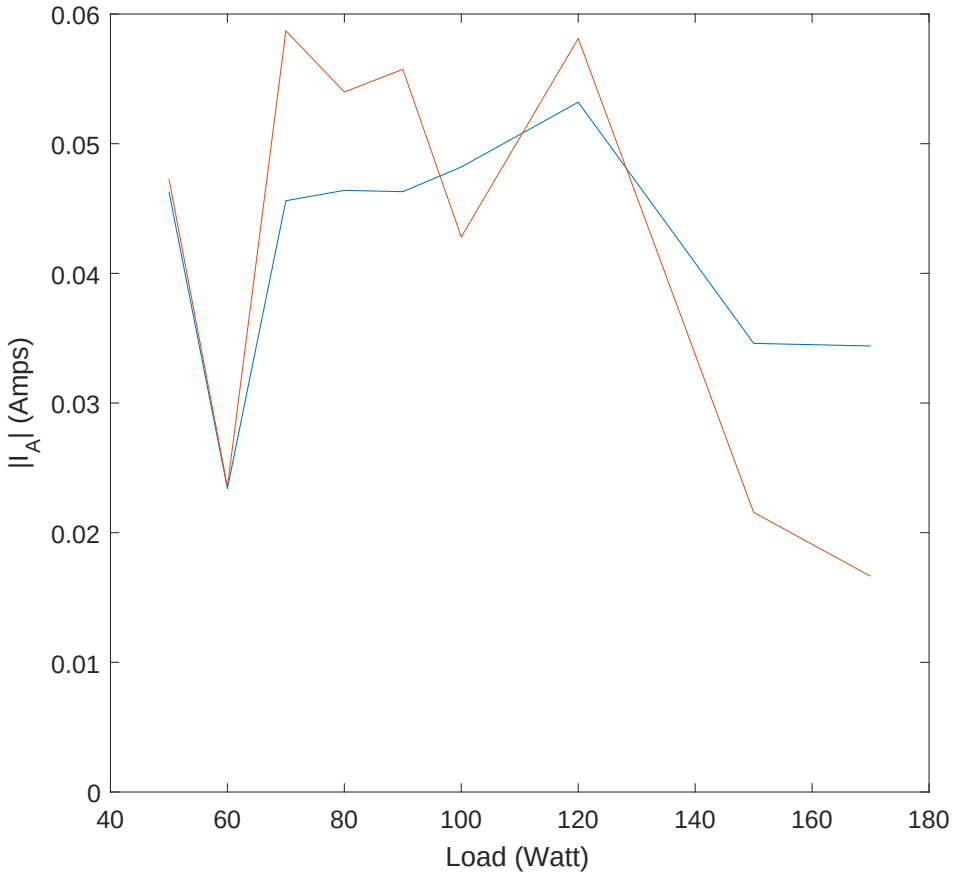

Figure 4.27: Blue: Amplitude detected by proposed algorithm using aggregate current of fault induced Motor 2. Red: DFT of Motor 2 eccentricity signal from individual CT1.

CHAPTER 5: CONCLUSION

Although the tracking algorithm developed in this thesis gives better results where DFT of the signal cannot distinguish two rotor eccentricities there are some load cases where the results of the algorithm deviate by 0.01 Hz. However even with this deviation the two motor eccentricities can be easily distinguished by the algorithm.

It should be noted that when MCSA is employed to find faults in a motor, exact amplitude limits are not utilized. The fault amplitude limits are defined as a percentage of healthy motor amplitude. Hence a rough estimation (amplitudes measured by the algorithm is within 0.01 Amperes) should be sufficient to identify faults in the motor.

When loads are nearly identical as well, the tracking algorithm is able to identify two different rotor eccentricity frequencies and their amplitudes belonging to Motor 1 and Motor 2. This experiment was done for 1 minute and 2 minutes of motor data length, however the tracking algorithm can be exploited to run continuously on a slight lag (i.e the algorithm displays results x minutes after the input, albeit continuously) for on-line monitoring of motors.

Further testing of the algorithm will be done in an operational power plant to observe if the tracking algorithm measured amplitude and frequency is precise enough to clearly distinguish faults of two identical motors. However when the algorithm is pushed to detect multiple motor faults, initial measurement of their fault frequencies may be required to tie these frequencies with individual motors. Artificial intelligence and neural networks can then be employed to help distinguish multiple motors better and to identify fault frequencies and their amplitudes even when they deviate due to heat or other external factors, a condition which is not explored in this thesis.

REFERENCES

[1] D. Matic, F. Kulic, M. Pineda-Sanchez, and J. Pons-Llinares, "Artificial Neural Networks Eccentricity Fault Detection of Induction Motor," in *Computing in the Global Information Technology (ICCGI)*, 2010.

[2] W. T. Thomson and M. Fenger, "Current Signature Analysis to Detect Induction Motor Faults," *IEEE Industry Applications Magazine*, vol. 7, no. 4, pp. 26–34, 2001.

[3] A. E. Fitzgerald, J. Charles Kingsley, and S. D. Umans, *Electric Machinery.* Boston, McGraw-Hill Higher Education, 6^{th} ed., 2003.

[4] J. R. Stack, T. G. Habetler, and R. G. Harley, "Fault Classification and Fault Signature Production for Rolling Element Bearings in Electric Machines," in *4th IEEE International Symposium on Diagnostics for Electric Machines, Power Electronics and Drives, 2003. SDEMPED 2003.*, pp. 172–176, Aug 2003.

[5] T. C. Publishing, "The importance of electric motor drives." Online Article.

[6] J. P. G. De Abreu and A. E. Emanuel, "Induction Motor Thermal Aging Caused by Voltage Distortion and Imbalance: Loss of Useful Life and Its Estimated Cost," in *Papers Presented at the 2001 Annual Meeting. 2001 IEEE*, pp. 105–114, IEEE, 2001.

[7] B. Mortan, "Factoring In Condition Monitoring's Real Costs," *North American Windpower*, 2013.

[8] P. Alger, *Induction Machines: Their Behavior and Uses.* Gordon and Breach, 1995.

[9] I. Culbert, J. Oliver, and W. Johnson, "Random Wound Motor Failure Investigation," Tech. Rep. 1000898, EPRI, 2000.

[10] "Report of Large Motor Reliability Survey of Industrial and Commercial Installations, Part I," *IEEE Transactions on Industry Applications*, vol. IA-21, pp. 853–864, July 1985.

[11] "Report of Large Motor Reliability Survey of Industrial and Commercial Installations, Part II," *IEEE Transactions on Industry Applications*, vol. IA-21, pp. 865–872, July 1985.

[12] P. Albrecht, J. Appiarius, R. McCoy, E. Owen, and D. Sharma, "Assessment of the Reliability of Motors in Utility Applications-Updated," *IEEE Transactions on Energy Conversion*, no. 1, pp. 39–46, 1986.

[13] P. Albrecht, J. Appiarius, E. Cornell, D. Houghtaling, R. McCoy, E. Owen, and D. Sharma, "Assessment of the Reliability of Motors in Utility Applications," *IEEE transactions on energy conversion*, no. 3, pp. 396–406, 1987.

[14] G. Electric, "*Bently Nevada Asset Condition Monitoring Electric Motor Condition Monitoring and Protection Application Guide*." Application Note, [Online]. Available: https://www.orbit-magazine.com/wp-content/uploads/2016/03/GEA32339-Elec-Motor-Cond-Monit-App-Guide_R3.pdf, 2015.

[15] ABB, "*Condition Monitoring Solutions for Motors and Generators*." White Paper, [Online]. Available: https://library.e.abb.com, 2012.

[16] C. R. Mason, *The Art and Science of Protective Relaying*, vol. 195. Wiley, 1956.

[17] S. Grubic, J. M. Aller, B. Lu, and T. G. Habetler, "A survey on testing and monitoring methods for stator insulation systems of low-voltage induction machines focusing on turn insulation problems," *IEEE Transactions on Industrial Electronics*, vol. 55, no. 12, pp. 4127–4136, 2008.

[18] S. Nandi, H. A. Toliyat, and X. Li, "Condition Monitoring and Fault Diagnosis of Electrical Motors - A Review," *IEEE transactions on energy conversion*, vol. 20, no. 4, pp. 719–729, 2005.

[19] SKF, "*SKF Online Motor Analysis System - NetEP Software*." [Online]. Available: http://www.skf.com/us/knowledge-centre/media-library/index.html#tcm:12-155453, 2014.

[20] R. H. Park, "Two-Reaction Theory of Synchronous Machines Generalized Method of Analysis-Part I," *Transactions of the American Institute of Electrical Engineers*, vol. 48, no. 3, pp. 716–727, 1929.

[21] R. Park, "Two-Reaction Theory of Synchronous Machines-II," *Transactions of the American Institute of Electrical Engineers*, vol. 52, no. 2, pp. 352–354, 1933.

[22] W. T. Thomson and R. J. Gilmore, "Motor Current Signature Analysis to Detect Faults in Induction Motor Drives–Fundamentals, Data Interpretation, and Industrial Case Histories," in *Proceedings of 32nd Turbo machinery Symposium, A&M University, Texas, USA*, 2003.

[23] W. T. Thomson and A. Barbour, "On-Line Current Monitoring and Application of a Finite Element Method to Predict the Level of Static Air-gap Eccentricity in Three-Phase Induction Motors," *IEEE Transactions on Energy Conversion*, vol. 13, pp. 347–357, Dec 1998.

[24] R. A. Collacott, *Vibration Monitoring and Diagnosis: Techniques for cost-effective plant maintenance*. Halsted Press, 1979.

[25] J. R. Stack, T. G. Habetler, and R. G. Harley, "Fault Classification and Fault Signature Production for Rolling Element Bearings in Electric Machines," *IEEE Transactions on Industry Applications*, vol. 40, no. 3, pp. 735–739, 2004.

[26] M. E. H. Benbouzid, "A Review of Induction Motors Signature Analysis as a Medium for Faults Detection," *IEEE transactions on industrial electronics*, vol. 47, no. 5, pp. 984–993, 2000.

[27] U. Orji, C. Schantz, D. E. Barber, S. B. Leeb, R. Cox, J. Goshorn, and K. Thomas, "Electrical-Based Condition Monitoring Using Shaft Speed Oscillation Harmonics," *ASNE Day*, 2011.

[28] A. V. Oppenheim and R. W. Schafer, *Discrete-Time Signal Processing (3rd Edition)*. Prentice Hall Upper Saddle River, NJ, 2010, 3 ed., Aug. 2009.

[29] S. B. Leeb, *A Conjoint Pattern Recognition Approach to Nonintrusive Load Monitoring*. PhD thesis, Massachusetts Institute of Technology, 1993.

[30] D. Luo, S. Leeb, and L. Norford, "Instrumentation for High Performance Nonintrusive Electrical Load Monitoring," *Journal of Solar Energy Engineering*, 1998.

[31] A. E. Fuller, "Harmonic Approaches To Non-Intrusive Load Diagnostics," Master's thesis, Massachusetts Institute of Technology, 2008.

[32] V. P. Tran, *Methods for Improving Stability and Power Quality in Networks With High Levels of Power Electronics*. PhD thesis, The University of North Carolina at Charlotte, 2011.

APPENDIX A: MATLAB CODE OF PROPOSED ALGORITHM

```
clear;
fs = 120;
scale = 2.7023e-04;
x = load('file_number.prep');
i0x = x(:,1)*(1/64)*(1.25/2^12)
            *(1/110)*1000*(1/sqrt(2));
i0 = i0x - mean(i0x);
N = fs/0.001;
iw = hanning(length(i0)).*i0;
X = fft(iw,N);
X = X(1:N/2);
X = X*scale; %*(mean(i0x)/max(abs(X)));
freq = (0:N/2-1)*(fs/N); %fs/length=delta_f

figure,plot(freq,abs(X));
xlabel('Frequency (Hz)','FontSize', 14);
ylabel('|I_{A}| (Amp)','FontSize', 14);

L = size(i0,1);
t = (0:L-1)*(1/fs);

fi =0;
for f = 29.9:0.001:30
fi= fi+1;
p(fi) = mean(cos(2*pi*f*t)*i0);
```

```
q(fi) = mean(sin(2*pi*f*t)*i0);
s(fi) = p(fi)^2+q(fi)^2;
end
fk = 29.9:0.001:30;
%figure, plot(fk,s);
[ms,indxf] = max(s);
fc1 = fk(indxf)

mq = mean(sin(2*pi*fc1*t)*i0);
fi =0;
fi2=0;
for ph = -pi:0.001:pi
fi= fi+1;
%r(fi) = cos(2*pi*fc*t+ph)*i0';
r(fi) = mean(cos(2*pi*fc1*t+ph)*i0);
%u(fi) = mean(sin(2*pi*fc*t+ph)*i0);
end
ph = -pi:0.001:pi;
%figure, plot(ph,r);
[mr,indxr] = max(r);
ph1 = ph(indxr);
mu = mean(sin(2*pi*fc1*t+ph1)*i0);
%[mu,indxu] = max(u);
mag1 = 2*(sqrt(mr^2+mu^2))/L

i0fc = mag1*cos(2*pi*fc1*t+ph1);
i0f = i0fc';
```

```
i0n = i0-i0f;
N = fs/0.001;
iw = hanning(length(i0n)).*i0n;
X = fft(iw,N);
X = X(1:N/2);
freq = (0:N/2-1)*(fs/N); %fs/length=delta_f
figure,plot(freq,abs(2*X/N));
xlabel('Frequency (Hz)','FontSize', 14);
ylabel('|I_{A}| (Amp)','FontSize', 14);
fin= 0;
for fn = 29.9:0.001:30
fin= fin+1;
pn(fin) = mean(cos(2*pi*fn*t)*iw);
qn(fin) = mean(sin(2*pi*fn*t)*iw);
sn(fin) = pn(fin)^2+qn(fin)^2;
end
fkn = 29.9:0.001:30;
%figure, plot(fkn,sn);
[ms,indxfn] = max(sn);
fc2 = fkn(indxfn)

for ph2 = -pi:0.001:pi
fi2= fi2+1;
%r(fi) = cos(2*pi*fc*t+ph)*i0';
r2(fi2) = mean(cos(2*pi*fc2*t+ph2)*i0);
%u(fi) = mean(sin(2*pi*fc*t+ph)*i0);
end
```

```
ph2 = -pi:0.001:pi;
%figure, plot(ph,r);
[mr2,indxr2] = max(r2);
phc2 = ph2(indxr2);
mu2 = mean(sin(2*pi*fc2*t+phc2)*i0);
mag2= 2*(sqrt(mr2^2+mu2^2))/L
```